Mesoscale simulations of gravity waves during the 2008–2009 major stratospheric sudden warming

Varavut Limpasuvan,[1] M. Joan Alexander,[2] Yvan J. Orsolini,[3] Dong L. Wu,[4] Ming Xue,[5] Jadwiga H. Richter,[6] and Chihoko Yamashita[6]

Received 12 October 2010; revised 8 May 2011; accepted 3 June 2011; published 3 September 2011.

[1] A series of 24 h mesoscale simulations (of 10 km horizontal and 400 m vertical resolution) are performed to examine the characteristics and forcing of gravity waves (GWs) relative to planetary waves (PWs) during the 2008–2009 major stratospheric sudden warming (SSW). Just prior to SSW occurrence, widespread westward propagating GWs are found along the vortex's edge and associated predominantly with major topographical features and strong near-surface winds. Momentum forcing due to GWs surpasses PW forcing in the upper stratosphere and tends to decelerate the polar westerly jet in excess of 30 m s^{-1} d^{-1}. With SSW onset, PWs dominate the momentum forcing, providing decelerative effects in excess of 50 m s^{-1} d^{-1} throughout the upper polar stratosphere. GWs related to topography become less widespread largely due to incipient wind reversal as the vortex starts to elongate. During the SSW maturation and early recovery, the polar vortex eventually splits and both wave signatures and forcing greatly subside. Nonetheless, during SSW, westward and eastward propagating GWs are found in the polar region and may be generated in situ by flow adjustment processes in the stratosphere or by secondary GW breaking. The simulated large-scale features agree well with those resolved in satellite observations and analysis products.

Citation: Limpasuvan, V., M. J. Alexander, Y. J. Orsolini, D. L. Wu, M. Xue, J. H. Richter, and C. Yamashita (2011), Mesoscale simulations of gravity waves during the 2008–2009 major stratospheric sudden warming, *J. Geophys. Res.*, *116*, D17104, doi:10.1029/2010JD015190.

1. Introduction

[2] During certain winters in the Northern Hemisphere (NH), the typically strong circumpolar flow of the stratospheric polar vortex can abruptly weaken or reverse direction. Rapid warming of the stratospheric polar region accompanies this anomalous wind event, referred to as stratospheric sudden warming (SSW) [*Andrews et al.*, 1987]. When wind reversal (in a zonally averaged sense) appears at the 10 hPa level (~30 km), the event is characterized as a "major" SSW according to the World Meteorological Organization (WMO) definition. Historically, major SSWs occur about 6 times every 10 years [*Charlton et al.*, 2007]; however, their occurrence is neither periodic nor easily predicted. During a major SSW, the polar vortex undergoes a strong displacement off the pole or splits into two smaller vortices. For example, the major SSW in January 2006 (2009) was associated with vortex displacement (vortex split) [*Manney et al.*, 2009a].

[3] Such strong polar variability during SSWs is traditionally linked to the presence of planetary waves (PWs) and their interactions with the circumpolar flow [e.g., *Matsuno*, 1971; *Andrews et al.*, 1987]. Climatologically, PWs propagate predominately from the midlatitude to high-latitude winter troposphere and refract equatorward as they penetrate into the upper stratosphere. During SSWs, PW amplitude can greatly amplify and PW propagation tends to shift poleward before being refracted equatorward. Convergence of PW momentum and heat flux can strongly decelerate the polar night jet and induce a strong (residual) descent motion over the pole that contributes to the adiabatic warming of the stratospheric polar region. The interactions between PWs and the circumpolar flow strongly impact the synoptic evolution of the vortex. Sheets of tropical air and smaller anticyclones have been noted to be advected around the vortex's edge and over the pole [e.g., *O'Neill et al.*, 1994; *Manney et al.*, 2009b].

[4] However, the wintertime polar middle atmosphere is also teeming with much smaller scale gravity waves (GWs). These waves are generated near the surface (by processes like convection, flow over topography) or in situ in the

[1]Department of Applied Physics, Coastal Carolina University, Conway, South Carolina, USA.
[2]Colorado Research Associates Division, Northwest Research Associates, Boulder, Colorado, USA.
[3]Norwegian Institute for Air Research, Kjeller, Norway.
[4]Jet Propulsion Laboratory, California Institute of Technology, Pasadena, California, USA.
[5]Center for Analysis and Prediction of Storms and School of Meteorology, University of Oklahoma, Norman, Oklahoma, USA.
[6]National Center for Atmospheric Research, Boulder, Colorado, USA.

0148-0227/11/2010JD015190

middle atmosphere [e.g., *Sato*, 2000; *Fritts and Alexander*, 2003; *Yamashita et al.*, 2010]. In the mesosphere, dissipation of GW and the resulting drag that it induces on the circulation were recognized very early on as being crucial in closing off the winter polar westerly jet and the summer easterly jet, as well as in maintaining the polar atmospheric thermal structure [e.g., *Leovy*, 1964]. Observations using quasi-Lagrangian balloons, radiosondes [e.g., *Sato and Yoshiki*, 2008], and recent satellite observations [e.g., *Wu*, 2004] readily report ubiquitous GW activities in the stratosphere [e.g., *Alexander*, 2010, and references therein].

[5] To date, the roles of GWs in the stratosphere are still unclear. Decelerative effects of orographically generated GWs (OGWs) on the polar stratospheric flow can be sizable. Studies like those by *Watanabe et al.* [2006], *Limpasuvan et al.* [2007], and *Alexander et al.* [2009] indicated that local damping of OGWs in the upper stratosphere can retard the background flow in excess of 30 m s^{-1} d^{-1}. In global climate models (GCMs) with parameterized GW effects, GW drag in the stratosphere (in addition to the mesosphere) is important for these models to mimic observed stratospheric temperatures [e.g., *Garcia and Boville*, 1994].

[6] In particular, GW responses and behaviors to the overall polar vortex variability and SSWs are still unclear. Based on early GCM simulations that included the middle atmosphere, *Pawson* [1997] suggested that GWs can trigger strong wintertime polar vortex disturbances, associated with rapid warming of the polar stratosphere. The importance of GW in SSW is further suggested by *Richter et al.* [2010] using the National Center for Atmosphere Research (NCAR) Whole Atmosphere Community Climate Model (WACCM) Version 3.5. In replacing the arbitrarily (and traditionally) specified GW source spectrum parameterization with multiple schemes that account for various possible sources (frontal genesis, convection, and orography) linked to model-generated tropospheric quantities, these authors were able to improve simulations of the wintertime stratospheric circulation. In particular, the inclusion of a parameterization to estimate mountain stresses due to unresolved orography contributed largely to the model generation of SSW occurrence with frequencies comparable to observations. Furthermore, *Ren et al.* [2008] noted that the observed wind reversal (from westerly to easterly) during a major SSW can selectively allow eastward propagating GWs to impose an eastward drag in the mesosphere that leads to polar mesospheric cooling, as suggested by *Holton* [1983] and *Liu and Roble* [2002]. Alternatively, using a simple Holton-Mass model of stratospheric wave–mean flow interaction, *Birner and Williams* [2008] demonstrated that GWs may serve as small-scale variability (a la background "noise") that promotes SSWs. Defined as an additive noise term in the zonal momentum equation, small to moderate stochastic GW forcing can cause SSW to occur even when the PW activity alone is not sufficient to initiate SSW.

[7] To date, very few GW observations overlap with SSW occurrence. Using lidar (laser radar) temperature measurements in the stratosphere at Eureka (80°N, 86°W), *Duck et al.* [1998, 2001] noted enhanced GW perturbations along the vortex edge. Although based on few observations, these authors suggested that GW dissipation along the vortex's edge can induce a residual circulation that can substantially warm (through adiabatic descent) the stratopause/upper stratosphere region of the vortex core. *Venkat Ratnam et al.* [2004] used the Challenging Minisatellite Payload (CHAMP) Global Positioning Satellite (GPS) temperature profiles to observe GW during the unprecedented 2002 major SSW in the Southern Hemisphere (SH) related to the vortex split. Enhanced GW activity (about 3 times the climatological amount) was noted about 10 days prior to the onset of rapid temperature increase at the end of September. Like *Duck et al.* [1998], these authors noted GW enhancement near the vortex's edge [see also *Yamashita et al.*, 2010]. *Wang and Alexander* [2009] examined GW activity during multiple brief SSW events of 2008 using primarily GPS temperature profiles from the Constellation Observing System for Meteorology, Ionosphere and Climate (COSMIC) in addition to CHAMP. Three minor SSW events (i.e., warming without polar wind reversal) and one major SSW event were identified. Between 20 and 35 km levels, these authors noted enhanced stratospheric GW amplitudes at high NH latitudes during the warming episodes. They largely attributed this enhancement to the effects of the background flow during SSW on GW propagation. Particularly, the vertical wavelengths of the refracted GWs may be altered during these SSW events in such a way that increases their probability of being observed in GPS temperature profiles.

[8] To this end, the present paper examines NH gravity wave activities during the 2008–2009 major SSW through a series of mesoscale simulations. Unlike recent SSWs during the 2003–2004 and 2005–2006 winters, the 2008–2009 SSW event exhibits a clear-cut, polar zonal mean wind transition from westerly to easterly in January [see *Orsolini et al.*, 2010]. Zonal mean wind evolution during the 2003–2004 and 2005–2006 SSWs were characterized by the presence of easterlies interrupted by episodes of westerlies in the lower mesosphere as well as in the middle stratosphere. The 2008–2009 SSW event does not have such interruptions (at least at 70°N) and provides an ideal case to explore the relative characteristics and forcing of GW and PW in the presence of strong vortex variability and polar wind reversal. Complemented with an analysis product and satellite observations, these simulations illustrate that, prior to the occurrence of wind reversal, the strong vortex environment is dominated by westward propagating GW associated with major topographical features and strong near-surface winds. Breaking of these GWs in the upper stratosphere provides zonal mean decelerative effects in excess of 50 m s^{-1} d^{-1} that outweigh and precede PW forcing. As SSW occurs, topographically induced GWs are less prevalent due to the filtering effects of the incipient wind reversal, and PWs dominate the momentum forcing throughout the upper polar stratosphere. During SSW recovery, both PW and GW signatures were considerably weaker. Nonetheless, during SSW, eastward and westward propagating GWs are found and may be generated in situ by unbalanced flow adjustment processes. To this end, this paper provides an initial look into the possible GW evolution and its interplay with PW during a dramatic event in the middle atmosphere associated with a major SSW.

2. Data and Methodology

[9] In this study, we combine observations from satellite, meteorological fields from an analysis product, and simu-

lations from a mesoscale model to examine GWs during a major SSW event of January 2009. The geopotential height and temperature are observed by the NASA-EOS Aura *Microwave Limb Sounder* (MLS) whose vertical coverage ranges from the ground to about 90 km [*Waters et al.*, 2006] and covers approximately 85°S to 85°N. The effective horizontal resolution of these MLS data is about 200 km [*Schwartz et al.*, 2006]. These products are complemented by NASA's Goddard Earth Observing System analysis version 5 (GEOS-5) [*Rienecker et al.*, 2008]. Provided every 6 h, the GEOS-5 analysis are given on a 0.66° × 0.5° (longitude-latitude) grid and extend from the surface up to about 70 km [*Bloom et al.*, 2005]. At 60°N latitude, GEOS-5 longitude-latitude grid size corresponds to about 37 km (56 km) in the east–west (north–south) direction. Provided on isobaric levels, the analysis product has an equivalent vertical spacing of about 1 km starting at the 10 km level and increases to ~2 km at the 60 km level. Below 10 km, the data vertical resolution is less than 1 km. Therefore, stratospheric GWs of horizontal wavelength greater than ~150 km and vertical wavelength greater than ~8 km are potentially resolved in GEOS-5.

[10] Mesoscale simulations are performed using the University of Oklahoma's Advanced Regional Prediction Systems (ARPS) [*Xue et al.*, 2003]. Centered over the North Pole, the simulations are run at a 10 km horizontal resolution on a 9950 × 9950 km horizontal domain (995 × 995 grid points), using the polar stereographic map projection. Overall, the model domain covers the polar region out to about the 50°N latitude ring. The vertical grid spacing is 20 m in the lowest level and gradually increases with altitude to 400 m at 12 km, above which the vertical grid spacing remains fixed at 400 m. A rigid top boundary is set at 65 km (165 vertical grid levels in all). To minimize spurious wave reflections near the upper boundary, Rayleigh damping is imposed in the vertical starting at 55 km. The inverse of the *e*-folding timescale of damping gradually increases from zero at 55 km to 0.10 s^{-1} at the model's top. The presented results (below) are shown up to only 55 km to stay clear from the strongly imposed Rayleigh damping and possible rigid boundary effects. To maintain numerical stability, the model integration time step is set to 5 s. Each simulation run lasts 24 h, and model output is saved only every hour of simulation time due to its large size (~2 gigabyte/variable for each output). The initial and time-varying lateral boundary conditions for simulations are provided by the GEOS-5 analysis. GW disturbances are identified in the analysis and simulations from the raw (unfiltered) vertical winds and horizontal wind divergence. However, only horizontal wind divergence results are shown below.

[11] *Limpasuvan et al.* [2007] discussed the model and its setup in more detail. These authors used ARPS to simulate and validate realistic GWs over Greenland and the surrounding polar region during 24 January 2005. *Xue et al.* [2000] and *Doyle et al.* [2000] demonstrated the ability of ARPS to simulate orographically forced flow for idealized mountains and realistic terrain in producing intense downslope wind storms. Furthermore, *Horinouchi and Kosaka* [2002] extended ARPS up to the thermopause on a limited domain in the tropics to study convectively generated GWs propagating into the airglow region.

[12] The model's horizontal grids are provided on Cartesian coordinates. Polar stereographic projections are reflected in the ARPS governing equations. To facilitate our zonal mean analyses (such as the Eliassen and Palm flux), the model output is transformed from the model's computational coordinates to geophysical latitude-longitude coordinates of 0.1 degrees. This resolution is chosen to correspond to a zonal grid spacing of ~5 km at the lowest latitude (~50°N) in the model domain to over sample the model results of 10 km horizontal resolution. Results of the regridded model output in 0.1 degree longitude-latitude grid are then verified to be correct when compared to the ungridded results. Conservatively, the ARPS simulation can potentially reveal stratospheric GWs of horizontal wavelength greater than ~50 km and vertical wavelength greater than ~2 km.

3. The 2008–2009 SSW Zonal Mean Evolution

[13] To illustrate the relevant major SSW event, Figure 1a shows the time-altitude evolution of the zonal mean zonal wind ($\overline{u}$) and temperature ($\overline{T}$) at 70°N for December–March period from 2008 to 2009. Data from the GEOS analysis are shown in the top row and MLS observations in the bottom row. The MLS zonal wind is derived from the MLS geopotential height field using the geostrophic wind balance assumption [*Randel*, 1987]. Over the common altitude range (0–70 km), the analysis wind field is similar to observations. The zonal mean wind switches from westerly (red) to easterly (green/blue) around 20 January near 70 km. This wind reversal extends down to 10 hPa a few days thereafter, marking the occurrence of a major SSW based on the WMO definition. The polar easterlies eventually permeate down to the surface.

[14] The zonal mean polar temperature (Figure 1a, right) undergoes large changes near the stratopause as the westerly wind decelerates. The warm layer (reddish areas, marking the typical warm stratopause layer between 50 and 60 km) plunges into the troposphere as the polar region warms in coincidence with the appearance of the zero wind line (black contour). This descent leads to the apparent "separation" of the polar stratopause and the lowering of the mesospheric layer into the altitude range typically associated with climatological upper stratosphere, as noted by *Hitchman et al.* [1989] and *Orsolini et al.* [2010]. As the vortex recovers and the polar westerly again strengthens, this warm layer reforms and eventually returns to its pre-SSW position. The MLS stratopause recovers much slower than the GEOS analysis even though the duration of wind reversal is roughly similar. Notably, the MLS warm stratopause layer appears to be more elevated in mid-February. As remarked by *Manney et al.* [2009a], this difference suggests the importance of dynamical processes above 70 km in the vortex recovery not present in the analysis [*Limpasuvan et al.*, 2011]. Recall that the analysis product extends up to 70 km, whereas the MLS geopotential height and temperature are retrieved as high as 90 km. However, this difference may also be associated with the upper boundary condition in GEOS which tends to be relatively warmer than MLS near 0.1 hPa even before SSW. In MLS, anomalous mesospheric cooling around 80–90 km is clearly present in conjunction with the wind reversal [e.g., *Liu and Roble*, 2002; *Orsolini et al.*, 2010].

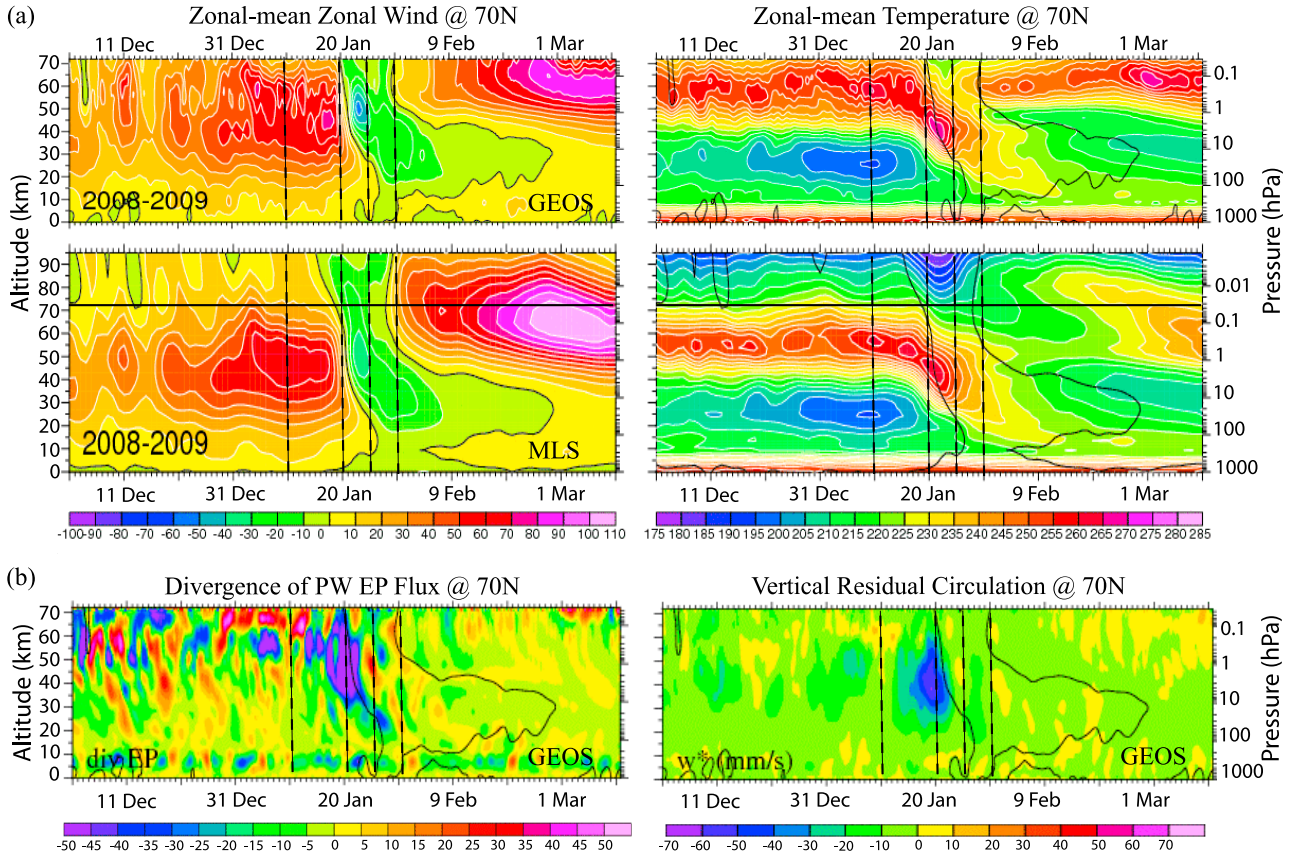

Figure 1. (a) The time-altitude evolution of the (left) zonal mean zonal wind and (right) zonal mean temperature at 70°N from the (top) GEOS-5 analyses and (bottom) MLS. (b) The time-altitude evolution of the (left) planetary wave Eliassen and Palm (EP) flux divergence (m s^{-1} d^{-1}) and (right) vertical residual circulation at 70°N from the GEOS-5 analyses. The black contour identities the zero zonal mean zonal wind. The dashed vertical lines indicate key dates in January 2009 (10, 20, 25, and 30 January) when model simulations are performed. The horizontal black line shows approximately the top level of GEOS.

[15] Despite this upper level deficiency of the GEOS analysis, the data is still useful for the model setup as described in section 2. While the ARPS model's top boundary extends up to 65 km, strong Rayleigh damping is applied above 55 km. Below 55 km, the GEOS analysis reproduces the MLS observations fairly well, so the product should serve well as the initial and boundary conditions for ARPS within the altitude of interest (0–55 km).

[16] Time evolution of PW forcing and the induced vertical residual motion at 70°N are shown in Figure 1b based on GEOS. Here, PWs are defined as disturbances of zonal wave number 1–4 and their mean flow influence is inferred from the divergence of their Eliassen and Palm (EP) flux. Following *Andrews et al.* [1987], the EP flux (***F***) is defined as a vector with meridional and vertical components ($F^{(\varphi)}$, $F^{(z)}$) given by

$$F^{(\varphi)} = \rho_o a \cos\varphi \left\{ \frac{\overline{u}_z}{\overline{\theta}_z} \overline{v'\theta'} - \overline{u'v'} \right\} \tag{1}$$

$$F^{(z)} = \rho_o a \cos\varphi \left\{ \frac{1}{\overline{\theta}_z} \left[f - \frac{(\overline{u}\cos\varphi)_\varphi}{a\cos\varphi} \right] \overline{v'\theta'} - \overline{u'w'} \right\}, \tag{2}$$

and its divergence,

$$\nabla \bullet F = (a\cos\varphi)^{-1} \frac{\partial}{\partial\varphi} \left(F^{(\varphi)} \cos\varphi \right) + \frac{\partial F^{(z)}}{\partial z}, \tag{3}$$

represents the wave-driven forcing of the zonal mean zonal wind. The variables in the above equations are based on the definitions established by *Andrews et al.* [1987]. In the EP flux components shown in (1) and (2), the vertical flux of zonal momentum ($\overline{u'w'}$) tends to be most relevant for GWs [e.g., *Alexander et al.*, 2010], and the other fluxes for PWs. While the PW flux divergence is noisy, we see (in Figure 1b) relatively weak and incoherent forcing prior to the SSW (e.g., at 10 January). Enhanced westward forcing (blue patches) appears just before the zonal mean westerly wind transitions to easterly, marking a period of large negative $\overline{u}$ tendency around 20 January. During this time, the westward forcing drives a strong polar descent motion (intense blue region in the residual vertical wind) in conjunction with the incipient descent of the warm stratopause layer. As this SSW event matures (e.g., 25 and 30 January), both the PW westward forcing and downward residual motion slightly

precede the zero wind line (black contour) and propagate downward.

4. Time-Averaged GW Signature and Forcing

[17] Four key dates will be examined during the 2008–2009 major SSW: 10, 20, 25, and 30 January (as marked by the vertical dashed lines in Figure 1). Each date provides a reasonable "snapshot" examination of the vortex prior to SSW through its eventual maturation and early recovery (as noted in section 3). For each key date, a 24 h mesoscale simulation, initialized during 0000 Coordinated Universal Time (UTC), is performed with the setup discussed in section 2. The time-averaged ARPS simulation for each date is computed from the hourly output, 6 h after initialization.

[18] Figures 2a–2d demonstrate the polar vortex evolution (based on geopotential heights) at different levels (~ 239, 57, and 3 hPa). The top, middle, and bottom rows of Figures 2a–2d display results from the daily averaged MLS observations, daily averaged GEOS analysis, and the time-averaged ARPS simulation, respectively. For each date, the geopotential height patterns are generally similar among the three data sets, and the horizontal winds are comparable between the analysis product and ARPS. For the most part, the observed large-scale flow was well simulated in the model.

[19] During 10 January (the "pre-SSW" period; Figure 2a), a well-formed, stratospheric vortex is nearly barotropic in altitude and slightly asymmetric with respect to the North Pole. A similar circumpolar flow (albeit weaker) is evident in the troposphere (239 hPa) with a vertically deep anticyclonic pattern over northern Europe that extends toward the Arctic Circle. In the analysis product and simulations, horizontal wind divergence is shown as solid contours. Coherent groupings of divergence (reddish band) and convergence (bluish band) smaller than planetary scale indicate possible GW presence. In GEOS, GWs appear at various locations around the globe, with most notable features at lower latitudes. For example, organized wave-like structures are apparent at all displayed levels over Western Canada and Scandinavia. With a much higher horizontal and vertical spatial resolution than the analysis product (see section 2), the ARPS simulation reveals stronger divergence patterns that are more locally focused geographically. Note that the GEOS color scale, as shown, is a factor of 10 smaller than ARPS. Such smaller contour interval of the GEOS field tends to accentuate divergence-convergence features at 240 hPa where local wind acceleration occurs due to tropospheric flow distortions. Furthermore, as noted above, the decreasing vertical resolution of GEOS with altitude may also affect the magnitudes of the resolved GWs in the analysis. Distinct wave packets over Greenland and Russia are easily identified in the simulation. The noted GW patterns in GEOS above Western Canada and Scandinavia are better resolved in the simulation.

[20] During 20 January (the "SSW onset" period; Figure 2b), the polar vortex has become elongated and varies considerably with altitude. The predominantly westerly (i.e., circumpolar) flow seen during 10 January has now evolved into a flow with considerable meridional (north–south) excursions. The zonal mean wind is weakened at nearly all altitudes, as suggested in Figure 1a. In the simulations, GWs are mostly present at 3 hPa, and the wave perturbations at this level are not readily traceable to the lower atmosphere due to strong vertical variation of the vortex. In the Eurasian region (near 90°E–120°E and 50°N), strong GW activities in simulations are captured in the analysis product (albeit much weaker) at nearly all levels. Similarly, GW features near 120°W and 60°N (Western Canada) are noted in both the analysis product and the ARPS simulations.

[21] The polar vortex elongation continues on 25 January (Figure 2c). The polar anticyclonic flow is now the attendant pattern at 3 hPa. With more prominent anticyclonic patterns in the stratosphere, the horizontal winds are now dominated by their easterly zonal component, consistent with the zonal mean zonal wind reversal evident in Figure 1a. Highly localized GW-like features are evident in the simulations near Eurasia, Eastern Russia, Greenland, and Western Canada. While not obvious, some of these features may have a counterpart in the analysis.

[22] During 30 January (the "late SSW" period; Figure 2d), the anticyclonic flow seen on 25 January continues to persist at 3 hPa. Lower down, the polar vortex has completely separated into two distinct cyclones, centered over Canada and Russia. Strong GW clusters near Western Canada (~120°W) and Eurasia (130°E) exist at 57 hPa and below in both the analysis and simulations. At 3 hPa, the time-averaged GW wave activities are nearly absent.

[23] To examine the time-averaged wave forcing, we perform EP flux analyses as given in equations (1)–(3). *Sato et al.* [1999] and *Watanabe et al.* [2008] used this formulation in diagnosing GW forcing with respect to PW. While diagnostics based on zonally averaging may potentially trivialize the presence of GW effects in the middle atmosphere due to the wave's localized nature (as seen in Figures 2a–2d), the EP flux analyses may still offer some insights on GW relative influence with respect to PW.

[24] In evaluating the relative importance of various atmospheric waves, the wave components are separated into two groups based on their zonal spatial scale. Planetary waves are defined as those disturbances of zonal wave number 1–4 (as done in section 3). We then categorize GWs as disturbances whose spatial scales are smaller than 1600 km [e.g., *Andrews et al.*, 1987; *Watanabe et al.*, 2006, 2008]. We note that at 80°N the present PW definition includes zonal wavelength longer than 1740 km which exclude GW. However, poleward of 80°N, this definition may include scales smaller than 1740 km. Experiments with changing the zonal wave number range from 1–3 to 1–5 in our PW definition did not significantly alter the results shown below.

[25] Figure 3 shows the EP flux (vectors) and its divergence (solid contours) time-averaged for each key date (rows) and wave category (columns). The zonal mean zonal wind is overlaid on each plot as line contours, with dashed contours denoting easterly wind. The EP flux vectors are scaled by the product of Earth's radius and density to accentuate wave activity in the middle atmosphere. The vector length is scaled with respect to that of 10 January to allow for the illustration of growth and decay. Overall, the strongest GW flux divergence occurs prior to SSW and precedes the strong PW flux divergence during SSW onset (20 January).

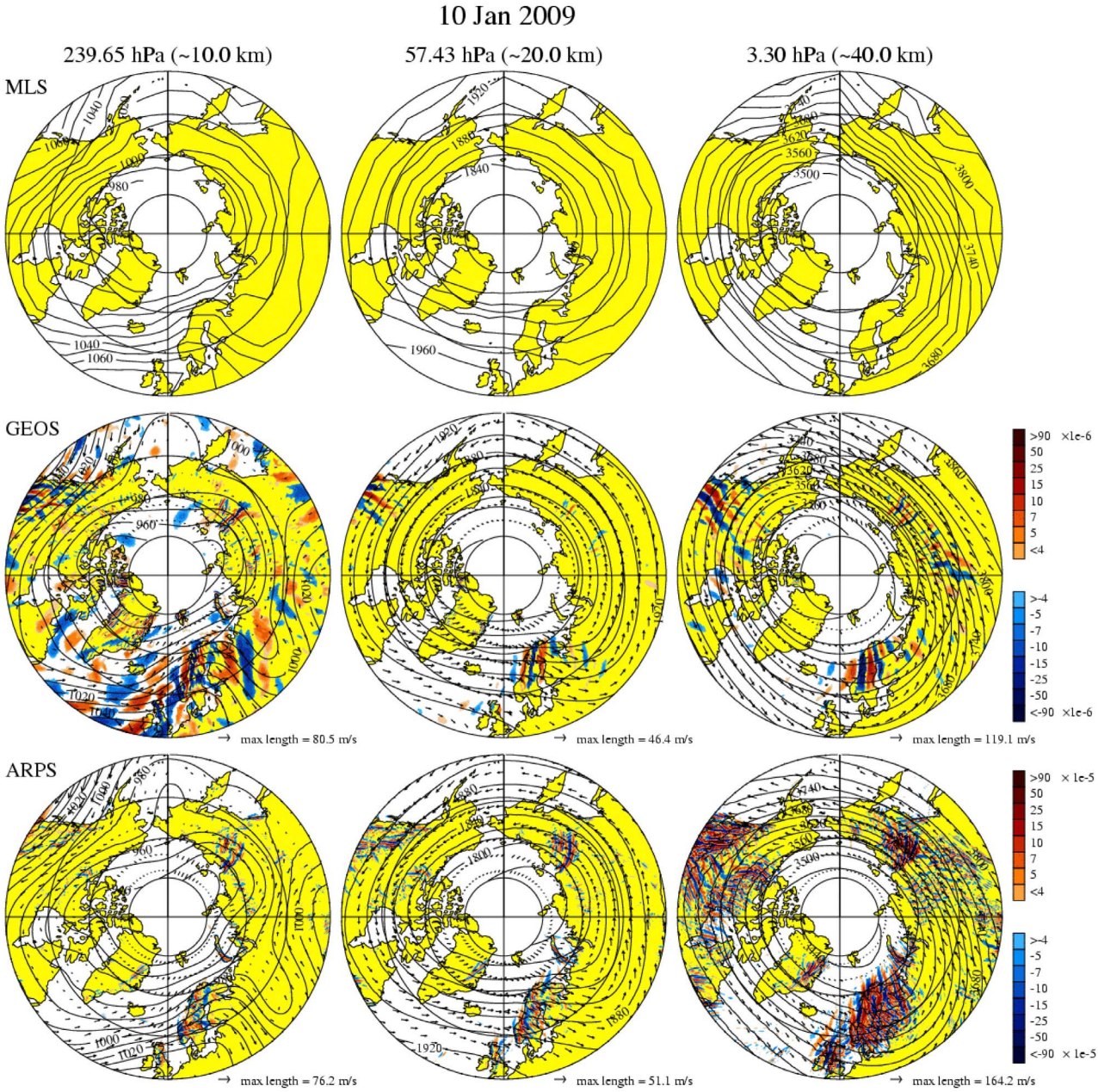

Figure 2a. Polar stereographic plots of daily averaged geopotential height (contour lines in decameter, dam) on 10 January 2009 near 239, 57, and 3.3 hPa levels from (top) MLS observations, (middle) GEOS analyses, and (bottom) ARPS simulation. The GEOS and ARPS results are shown with horizontal divergence (solid contours) along with horizontal winds (as vectors). Note that the GEOS divergence is derived by filtering out zonal spatial scale larger than 1,600 km, and its color scale is a factor of 10 smaller than ARPS. The underlying land areas are shown in yellow.

[26] To complement Figure 3, GW vertical flux of zonal momentum ($\overline{u'w'}$) for multiple bands of spatial scales (800–1600 km, 400–800 km, 100–400 km, and 50–100 km) is illustrated in Figure 4. The sums of these banded values indicate the total vertical flux of zonal momentum by GWs resolved in ARPS. As noted by *Watanabe et al.* [2008], the vertical EP flux component of GWs in equation (3) tends to be dominated by the ($\overline{u'w'}$) term. In NH polar night jet, upward EP flux component likely corresponds to the upward flux of westward momentum ($\overline{u'w'} < 0$) associated with GWs propagating westward relative to the zonal mean zonal wind. Damping of these GWs then results in deceleration of the mean wind. OGWs are nearly stationary relative to the ground but are generally westward propagating GWs relative to the flow.

[27] During 10 January, PW EP flux is modest in the stratosphere (Figure 3a, left). While most PW activity is refracted equatorward, slight bifurcation in the wave path

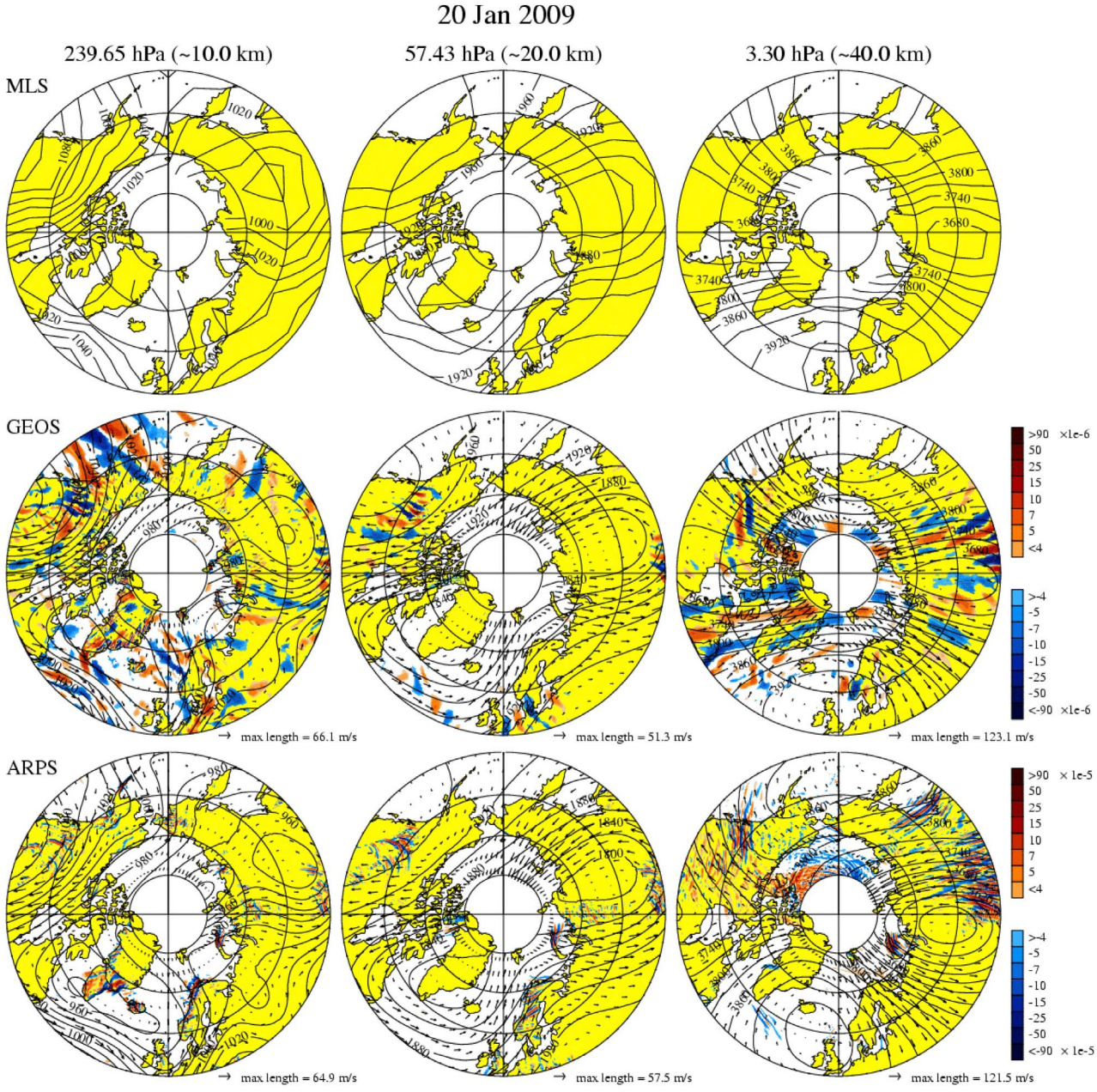

Figure 2b. Same as Figure 2a but for 20 January 2009.

appears near the lower part of the westerly jet core. Consequently, weaker EP flux divergence (orange color, peaking around 30 m s^{-1} d^{-1}) is evident at the jet core along with weak flux convergence (blue region; peaking around 30 m s^{-1} d^{-1}) on the poleward jet flank. The daily averaged PW EP flux and its divergence in the GEOS analyses on the same day produce similar results (not shown). The EP flux associated with GW (Figure 3a, right) resides mainly equatorward of 75°N and above 35 km. Propagating vertically upward, GW EP flux converges throughout the westerly jet core and exerts strong decelerative effects that can locally exceed 70 m s^{-1} d^{-1} (dark blue). However, localized pockets of strong GW EP flux divergence with accelerative effects greater than 50 m s^{-1} d^{-1} are also present. While GEOS analyses exhibit some GW-like disturbances (see Figures 2a–2d), the corresponding EP flux analyses reveal very much smaller flux vector and wave forcing. Figure 4a demonstrates that the GW activity is associated with westward propagating waves (blue patches) with the dominant spatial scale of 100–400 km. As seen in Figure 3, downward pointing GW EP flux is present between 50°N and 60°N despite the presence of negative ($\overline{u'w'}$) on 10 January. Closer examination reveals that the downward EP flux is due to large positive GW meridional heat flux ($\overline{v'\theta'}$) that dominate the region (not shown).

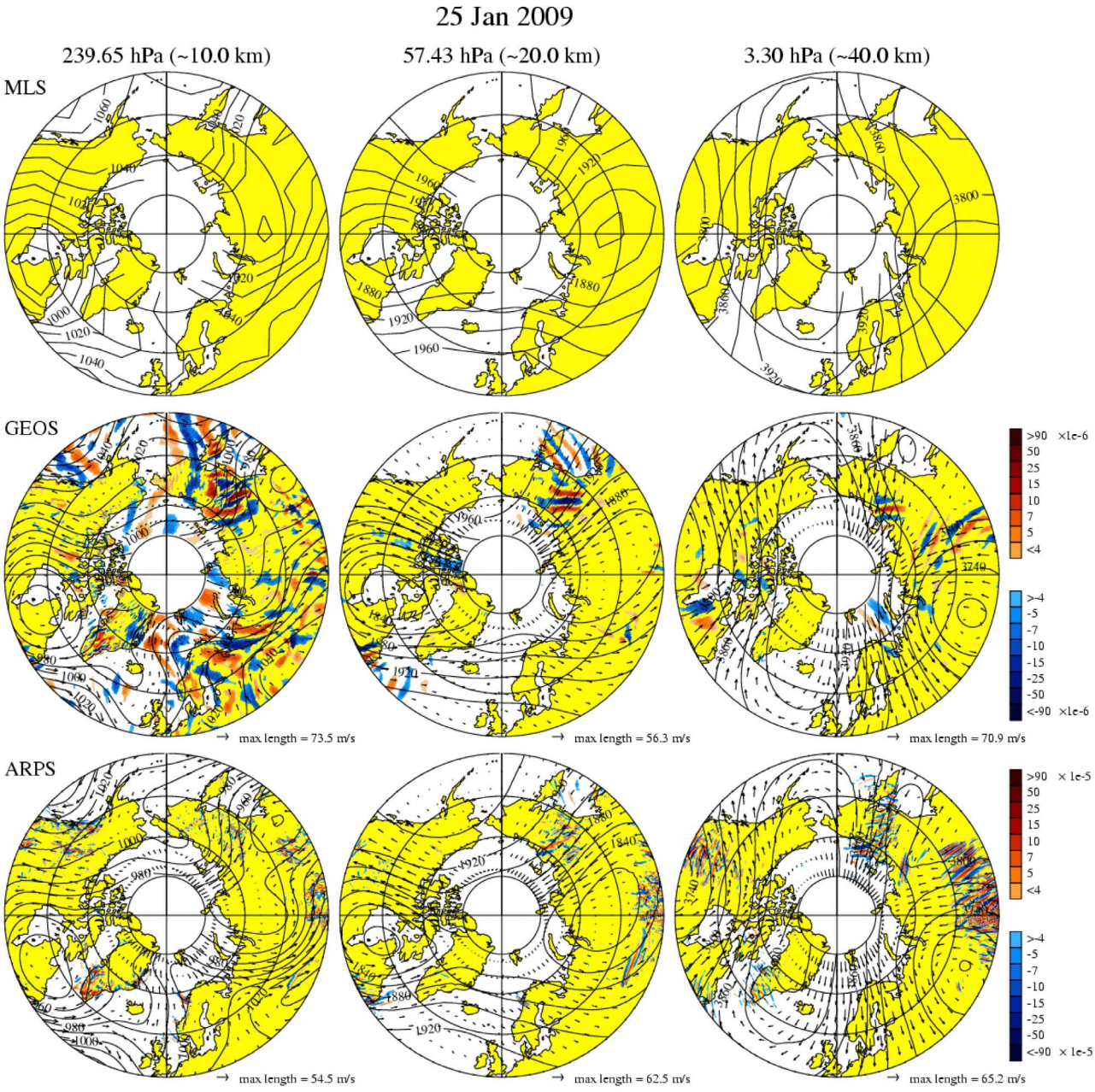

Figure 2c. Same as Figure 2a but for 25 January 2009.

[28] During the incipient stage of SSW (20 January), easterly winds in the upper stratosphere are clearly seen between 50°N and 75°N as the zero wind line dips to ~30 km at 50°N. The PW activity is overwhelmingly large compared to 10 January in the upper stratosphere. The PW presence is consistent with the dominance of wave number-2 characteristics noted in Figure 2b. Convergence of PW EP flux produces westward accelerations well above 50 m s^{-1} d^{-1}. At high latitudes, PW flux near 30 km emanates laterally from the polar region. The resulting flux divergence (near 80°N and the descended westerly jet core) generates eastward acceleration above 30 m s^{-1}. While this westward forcing may be an artifact of the model simulations, *Tomikawa* [2010] suggests that emanation of PW activity from the polar region is typical and may be a manifestation of jet barotropic/baroclinic instability related to the jet shear/curvature. The associated flux divergence from these PWs may provide accelerative forcing that regulates the persistence of the easterly wind during SSW [*Tomikawa*, 2010]. Indeed, computation of the meridional gradient of quasi-geostrophic potential vorticity from ARPS and GEOS zonal mean zonal wind indicates widespread pockets with negative values (a necessary condition for jet instability) at high latitude during this key date [*Charney and Stern*, 1962; *Andrews et al.*, 1987]. Planetary wave flux divergence computed from the GEOS analysis product indicates much weaker eastward acceleration in the polar region near 30 km.

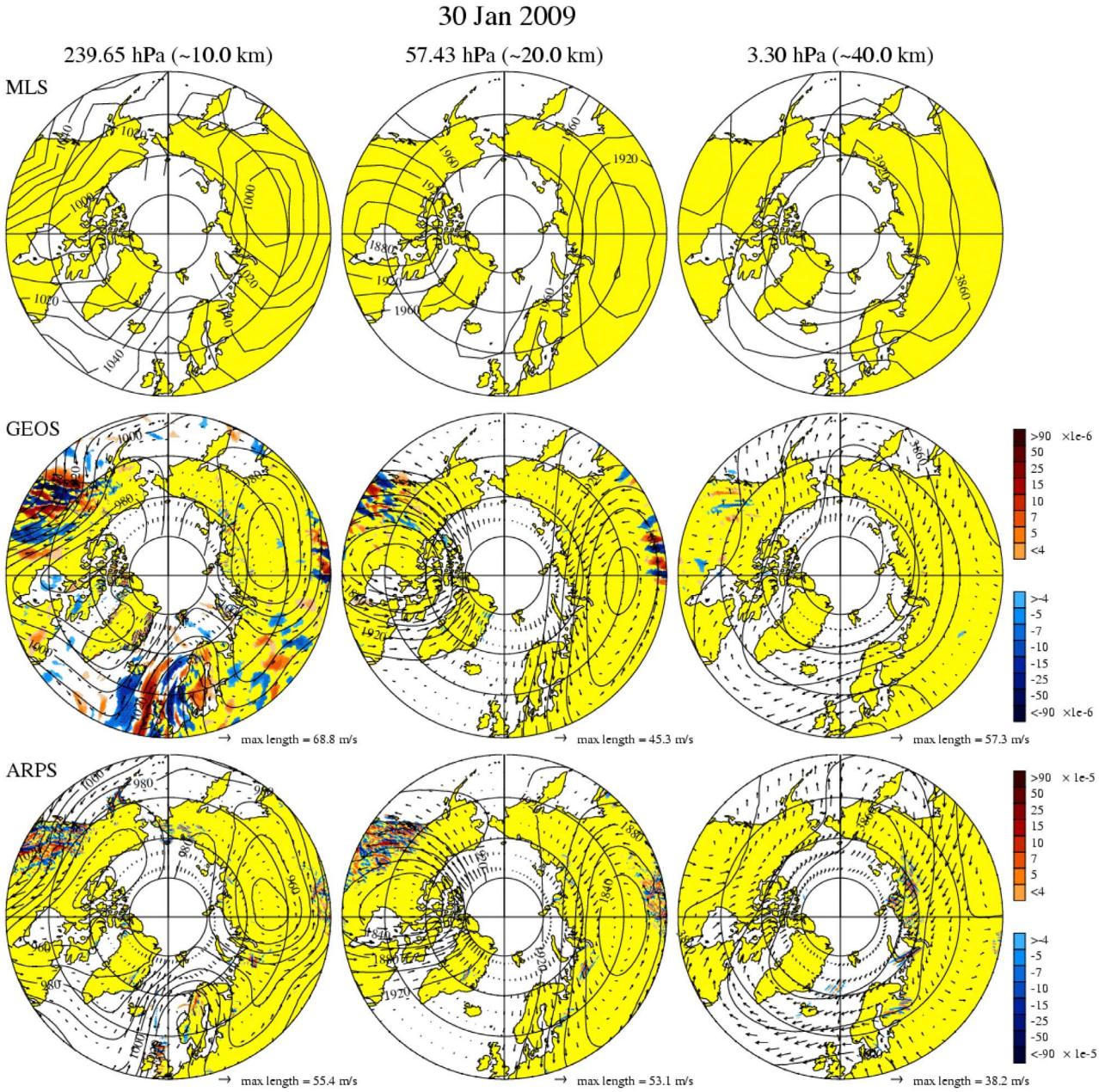

Figure 2d. Same as Figure 2a but for 30 January 2009.

[29] The upward GW activity persists in the upper stratosphere above the zero wind line on 20 January. While GW forcing provides much of the westward drag (relative to PW) on the westerly jet during 10 January, PW and GW act in concert to slow down the jet during SSW onset. Figure 4b shows that damping of westward propagating GWs (of 100–400 km and 800–1600 km spatial scales) near the easterly jet is responsible for the westward drag. Compared to 10 January, we note a more widespread presence of eastward propagating GWs (orange patches) in the polar stratosphere and near the surface. Below 12 km, the eastward propagating GWs around 65°N appear in conjunction with a cyclonic flow centered near the southern tip of Greenland (e.g., Figure 2b for 20 January at ~10 km).

[30] During the mid to late SSW stages (25 and 30 January), the enhanced EP flux convergence region tends to follow the zero wind line's descent as the easterly wind dominates the circulation above 25 km. The convergence of PW EP flux around 30 km provides decelerative effects in excess of 30 m s^{-1} d^{-1}. On 25 January, GW flux and its convergence are apparent in the easterly winds above 35 km between 50°N and 70°N (well above the zero wind line). The existence of GW flux convergence in the easterlies suggests that on the zonally averaged GW phase is moving westward with speed greater than 20 m s^{-1}. Most westward propagating GWs are confined mainly between 50°N and 60°N with a dominant 100–400 km spatial scale (Figure 4c). Eastward propagating GWs are found near the easterly jet core around 40 km. On

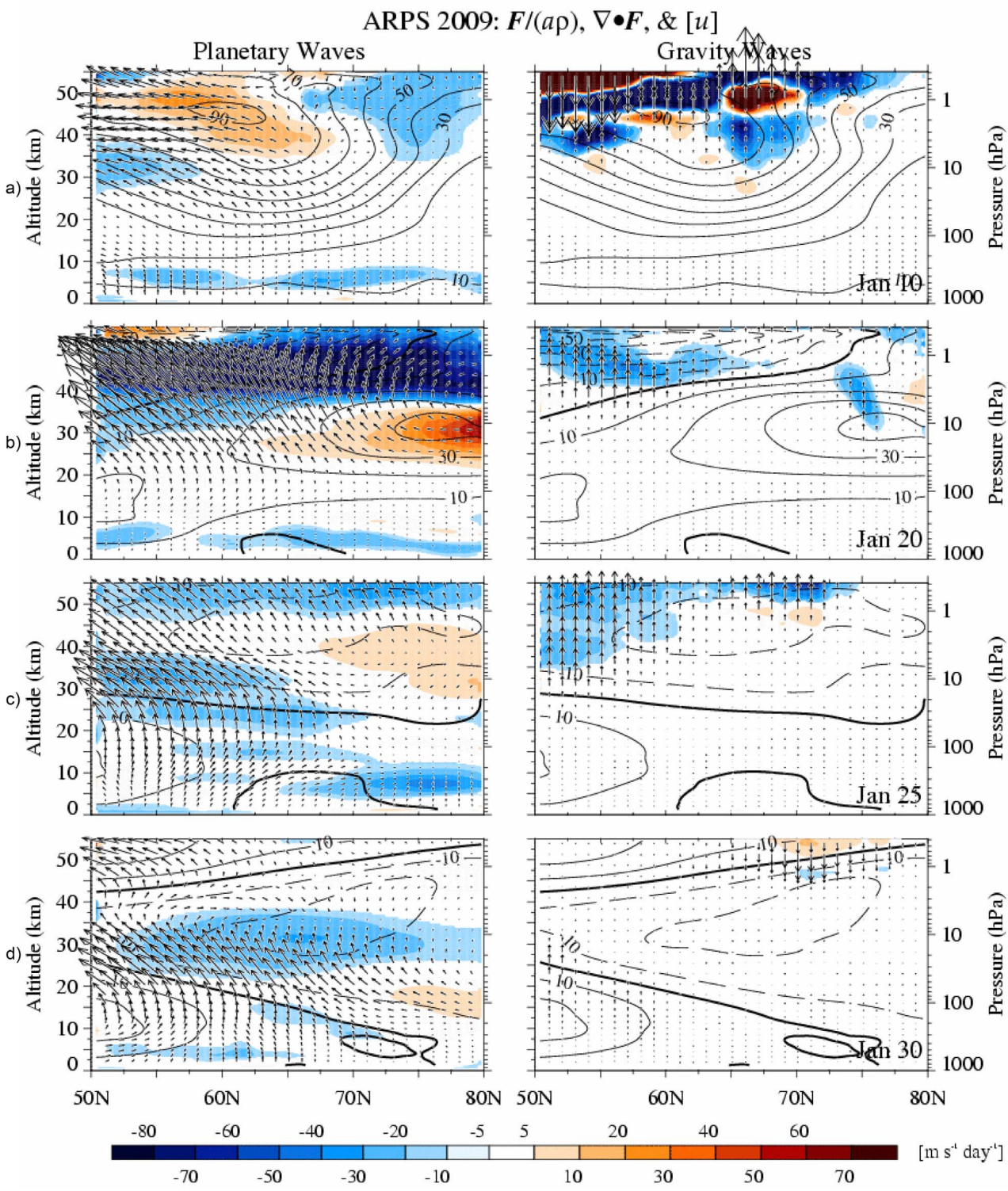

Figure 3. Time-averaged ARPS EP flux vectors (arrows) and EP flux divergence (solid contours) for (a) 10, (b) 20, (c) 25, and (d) 30 January 2009. Fluxes associated with (left) planetary waves (PWs) and (right) gravity waves (GWs) are shown. For presentation, the vertical component of the EP flux is multiplied by 250, and the vectors are divided by the product of Earth's radius and density to accentuate vectors in the middle atmosphere. Zonal mean zonal wind is overlaid as line contours at 10 m s^{-1} interval (with the zero wind line thickened).

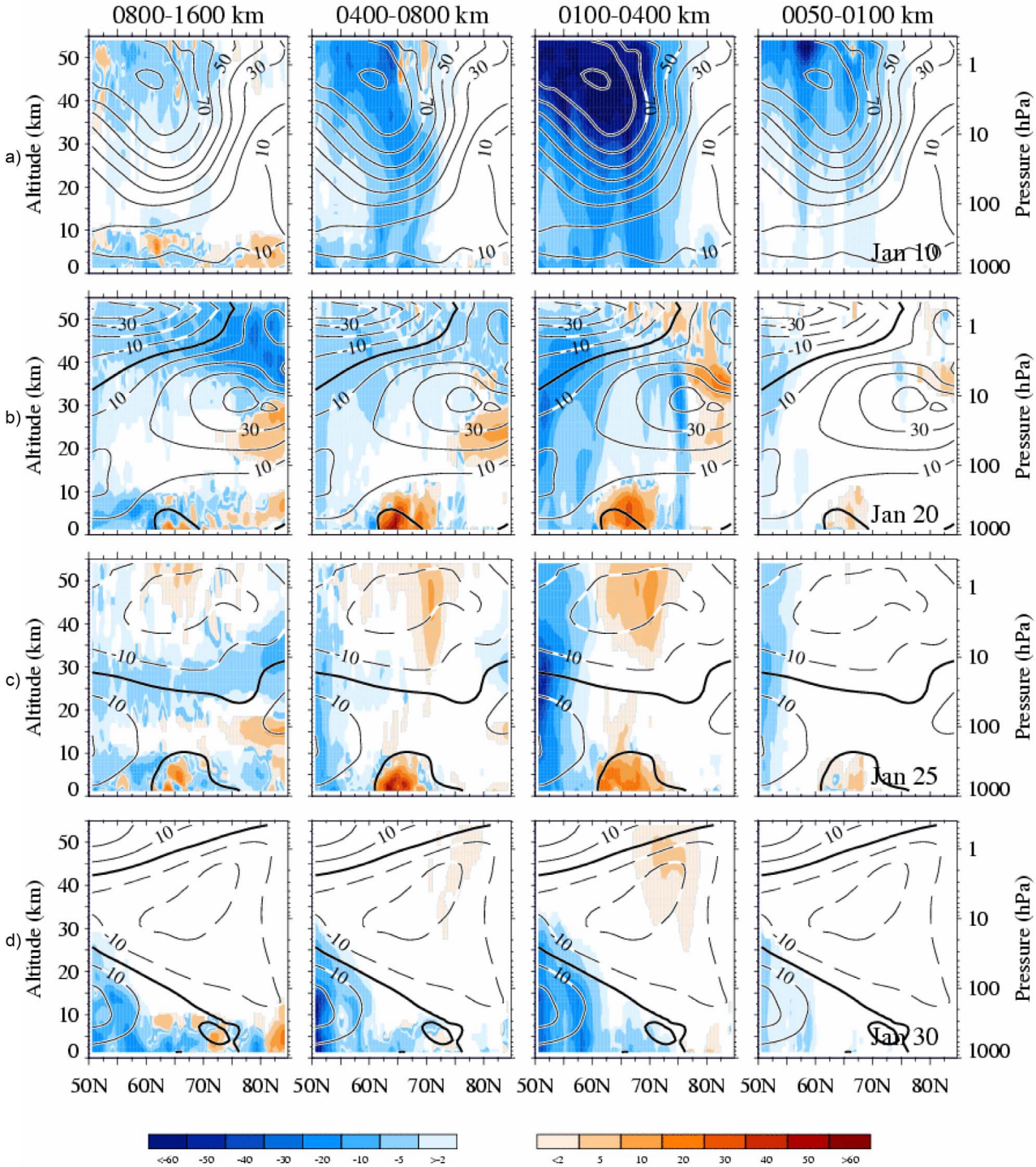

Figure 4. Time-averaged, zonal mean ARPS vertical flux of zonal momentum ($u\,w$; solid contours) for (a) 10, (b) 20, (c) 25, and (d) 30 January 2009. Flux is partitioned into various bands of spatial scales, as indicated by the top labels. For presentation, the flux is scaled by the square root of density to emphasize feature at all levels and is multiplied by 2000 for presentation. Zonal mean zonal wind is overlaid as line contours at 10 m s^{-1} interval (with the zero wind line thickened).

30 January, we note the correspondence between the eastward propagating GW (of 100–400 km scale) near the zero wind line at 50 km and the downward pointing EP flux vectors where the GW heat fluxes are weak. Overall, most GW fluxes predominantly occur in the 50°N–60°N latitude band after 10 January.

[31] Because of high computational cost, only a few selected dates are simulated during the 2008–2009 SSW

with focus placed on the key dates when the vortex undergoes marked transitions. A continuous examination of the wave forcings' time evolution and their interaction with the zonal mean circulation is not possible in the simulations. However, the altitude-time evolution of polar PW forcing in the GEOS analyses (shown in Figure 1b) demonstrates consistent results with the snapshots shown in Figure 3. In particular, we see relatively weak PW forcing prior to SSW (e.g., at 10 January) that greatly amplifies near the zero wind line during the SSW onset, driving strong polar descent motion. As warming matures, PW forcing propagates down in time, just before the zero wind line, as hinted in Figure 3.

[32] While GEOS reveal almost no noticeable GW effects, the present simulations suggest the roles of westward propagating GW in initially slowing down the westerly jet and in assisting the PW forcing as SSW transpires. During the mid to late SSW stages (25 and 30 January), the filtering effects of the zonal wind are evident in confining the westward propagating GWs at lower altitudes and allowing more eastward propagating GWs to become more prevalent as the easterly wind dominates the polar vortex. *Yamashita et al.* [2010] used the European Centre for Medium-Range Weather Forecasts (ECMWF T799) assimilated data to study GW energy variation during the same 2008–2009 SSW. This product has higher horizontal (0.25° × 0.25°) and comparable vertical resolution than GEOS but is coarser than ARPS. Over the altitude band of 65°N–70°N [see *Yamashita et al.*, 2010, Figure 4], we note that spatial scale dominance in GWs during SSW in ARPS is consistent with their results despite the limited sampling here. However, unlike GW energy, the sign of the vertical flux of horizontal momentum allow us to infer the propagation nature of the resolved GWs. With a horizontal resolution of 10 km, the ARPS can reveal GW features between 50 and 100 km spatial scales, not resolved by ECMWF. Figure 4 clearly shows that GWs of these finer scales can be quite strong, particularly prior to SSW onset. Moreover, while Figure 4 suggests that GWs of 100–400 km tend to be most dominant during these key dates, the extended time analyses of *Yamashita et al.* [2010] reveal that larger scale GWs (400–1600 km) can greatly amplify as SSW starts.

5. Detailed Looks at the Simulated GWs During Key Dates

[33] To elucidate the global distribution of vertical flux of zonal momentum, we define the overbar in computing $\overline{u'w'}$ as a 50 grid point running average in the zonal direction for each latitude. For our ARPS setup, this corresponds to a regional zonal average of about 5 degrees longitude. Figure 5 shows the global distribution of the vertical flux of zonal momentum at 1400 UTC for 10, 20, and 30 January, smoothed with a 20 grid point running average in both zonal and meridional direction. Scaled by the square root of density, the zonal mean of this distribution at multiple vertical levels produces the meridional cross sections similarly shown in Figure 4. In comparing Figure 5 with Figures 2a (bottom), 2b (bottom), 2c (bottom) and 2d (bottom), the $\overline{u'w'}$ distribution tend to encompass regions of pronounced GW divergence. However, the distribution also provides an indication of the zonal propagation of GWs relative to the local zonal wind and the region of upward wave activity. Negative fluxes (blue patches) indicate westward propagating GWs (relative to the local zonal wind) while positive fluxes (orange patches) eastward propagating GWs. In this section, we attempt to understand the possible GW sources in connection with the global fluxes. We note that *Sato et al.* [2009] recently used maps of $\overline{u'w'}$ to offer a global view of GW sources in the lower stratosphere [see also *Alexander et al.*, 2010].

5.1. Pre-SSW: 10 January 2009

[34] Figure 5a demonstrates the dominance of westward propagating GWs during 10 January emanating upward above topographical regions like the Rockies, Greenland, Scandinavia, and Eastern Russia. This dominance is consistent with results shown in Figure 4a. The time evolution (animation) of the corresponding GW divergence reveals these wave features to be quasi-stationary with respect to the ground. Therefore, the time-averaged divergence plot shown in Figure 2a (bottom) shows regions of GW activity above the aforementioned topographical features that resembles the instantaneous fluxes shown here at 1400 UTC.

[35] Figure 6 shows the longitude-altitude cross sections of horizontal wind divergence at 55°N and 65°N latitude circles on 10 January at 1000 and 2000 UTC. For each displayed section, the underlying topographic profiles (solid shapes) are shown as well as the zonal wind (line contours). The near-surface zonal wind is shown below the topographic profiles. The westward propagating GW features noted in the polar plots are seen as parts of wave packets that extend from identifiable underlying terrain features with moderately strong surface winds. Within these packets, the GW phases tilt mainly westward with altitude and the near-surface winds are predominately westerly. Smaller topographical features (like Novaya Zemlya Island, just north of Russia) have strong overlying wave perturbations when the near-surface wind speed is large. With the upward (and some zonal) extension of the packet at higher altitude, GW perturbations appear to be refracted toward longer vertical wavelength due to increasing wind speed (dark gray regions). Above 40 km, areas where the local Richardson number (*Ri*) is less than 0.25 (yellow areas) are found within these packets and indicate possible wave breaking (e.g., over Russia, Rockies) due to convective instability [*Fritts and Alexander*, 2003] near 50 km. Damping of GWs over these regions is consistent with the predominant areas of EP flux convergence and the associated decelerative effects shown in Figure 3a (right).

[36] Figure 7 shows cross-sectional close-ups of the time-averaged GW activities on 10 January near 120°W at 55°N ("Rockies") and 30°W at 70°N ("N. Greenland"). The time averaging period spans from 6 h after initialization (i.e., 0600 UTC) to the end of the simulation (2400 UTC) on 10 January. From the solid contours and ordinate tick marks, the alternation of the wave nodes (the transition between reddish to bluish areas) in the vertical provides an estimate of the simulated GW vertical wavelength. For the illustrated latitude, the spatial scale along the longitudinal direction is shown at the top abscissa of each cross section with respect to the Prime Meridian. The alternation of the wave nodes in the horizontal allows for estimates of the horizontal (zonal) wavelength. At the longitudinal location indicated by the vertical lines (near the center of the chosen domain), the

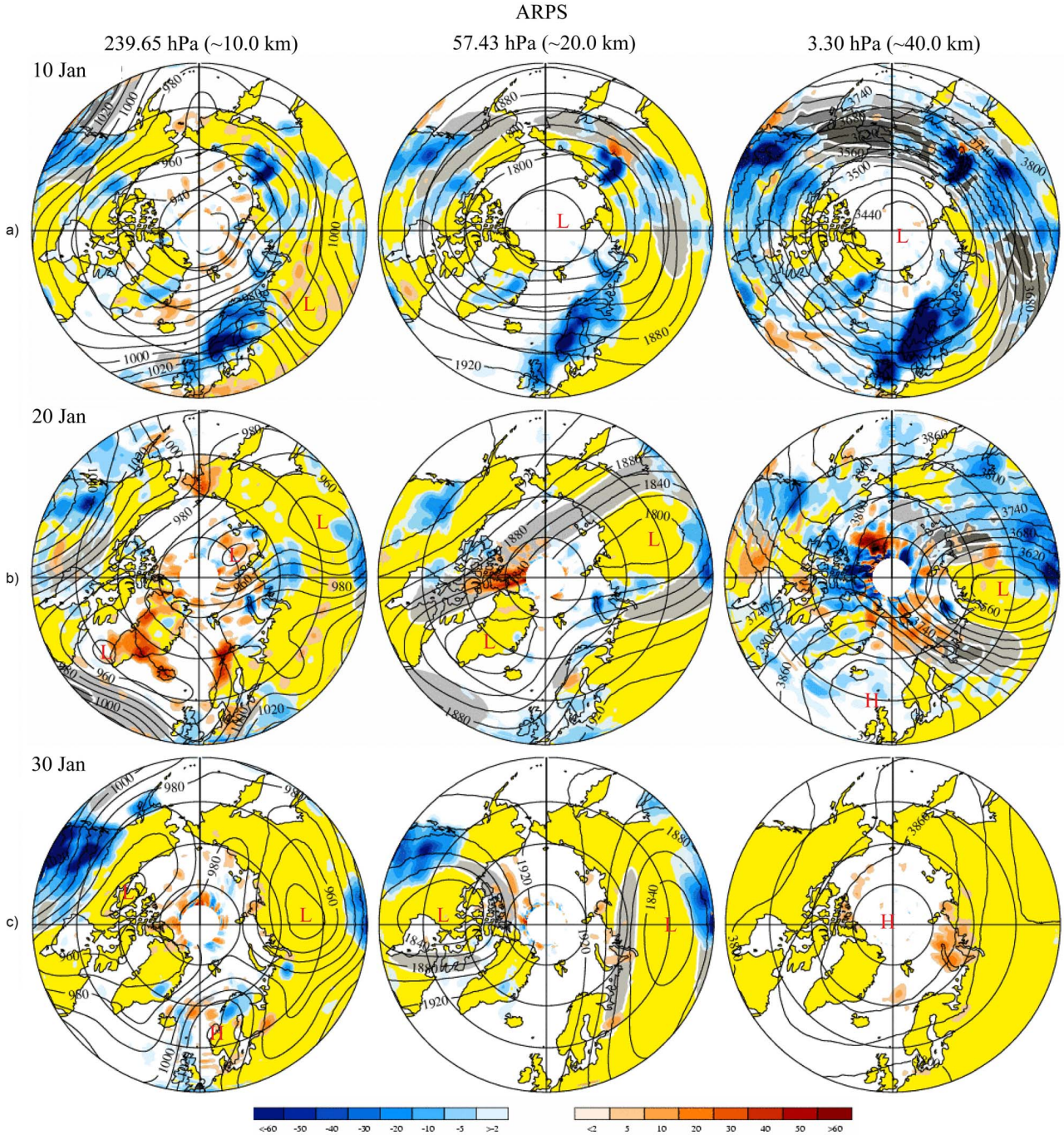

Figure 5. The polar distribution of GW vertical flux of zonal momentum (as solid contours) at 1400 UTC for three different isobaric levels (columns) for (a) 10, (b) 20, and (c) 30 January. The underlying land areas are shown in yellow. This is overlaid by successive darker gray-shaded regions identifying areas of strong horizontal wind speed (40, 60, and 80 m s^{-1} for left and middle columns; 80, 100, and 120 m s^{-1} for the right column). As solid contours, the GW vertical flux of zonal momentum is then superimposed on the plot. Finally, the geopotential heights are drawn as open contours.

vertical profiles of the zonal wind are shown in red, adjacent to the cross sections.

[37] In regions where the vertical zonal wind shear is small (i.e., the displayed wind profile is nearly vertical), we can estimate the GW's ground-based zonal phase speed (c_x), the vertical group velocity (c_{gz}), and the intrinsic (wind relative) wave frequency (ω) based on the wave's linear dispersion relation [cf. *Fritts and Alexander*, 2003]. At 55°N in the 30–40 km layer, the local zonal wind (u) is ~64.17 m s^{-1}, and the buoyancy frequency (N) is ~0.022405 s^{-1}. With the simulated horizontal and vertical wavelengths roughly about 160 km and 17.7 km (estimated

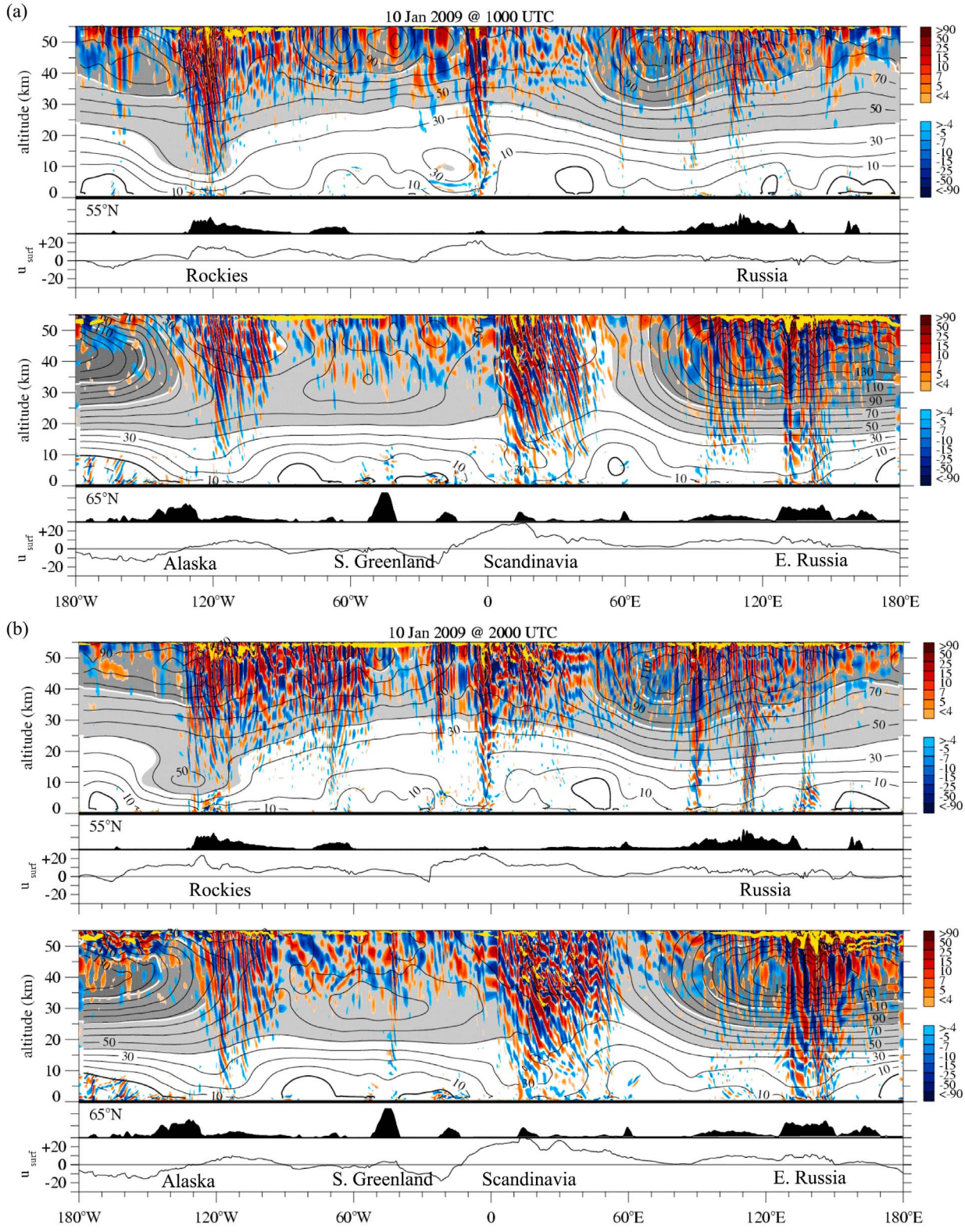

Figure 6. Altitude-longitude cross sections of the horizontal wind divergence as solid contours at (top) 55°N and (bottom) 65°N for 10 January at (a) 1000 UTC and (b) 2000 UTC. The zonal wind contours are overlaid as black lines at 10 m s^{-1} interval. The underlying terrain is shown as a black shape (every tick mark along the ordinate axis represents 1000 km). The zonal wind at the third model level ("u_{surf}") is shown below the terrain. Yellow regions indicate areas with the Richardson's number (*Ri*) less than 0.25. Successive darker gray regions identify areas of successive horizontal wind speed of 40, 80, and 120 m s^{-1}.

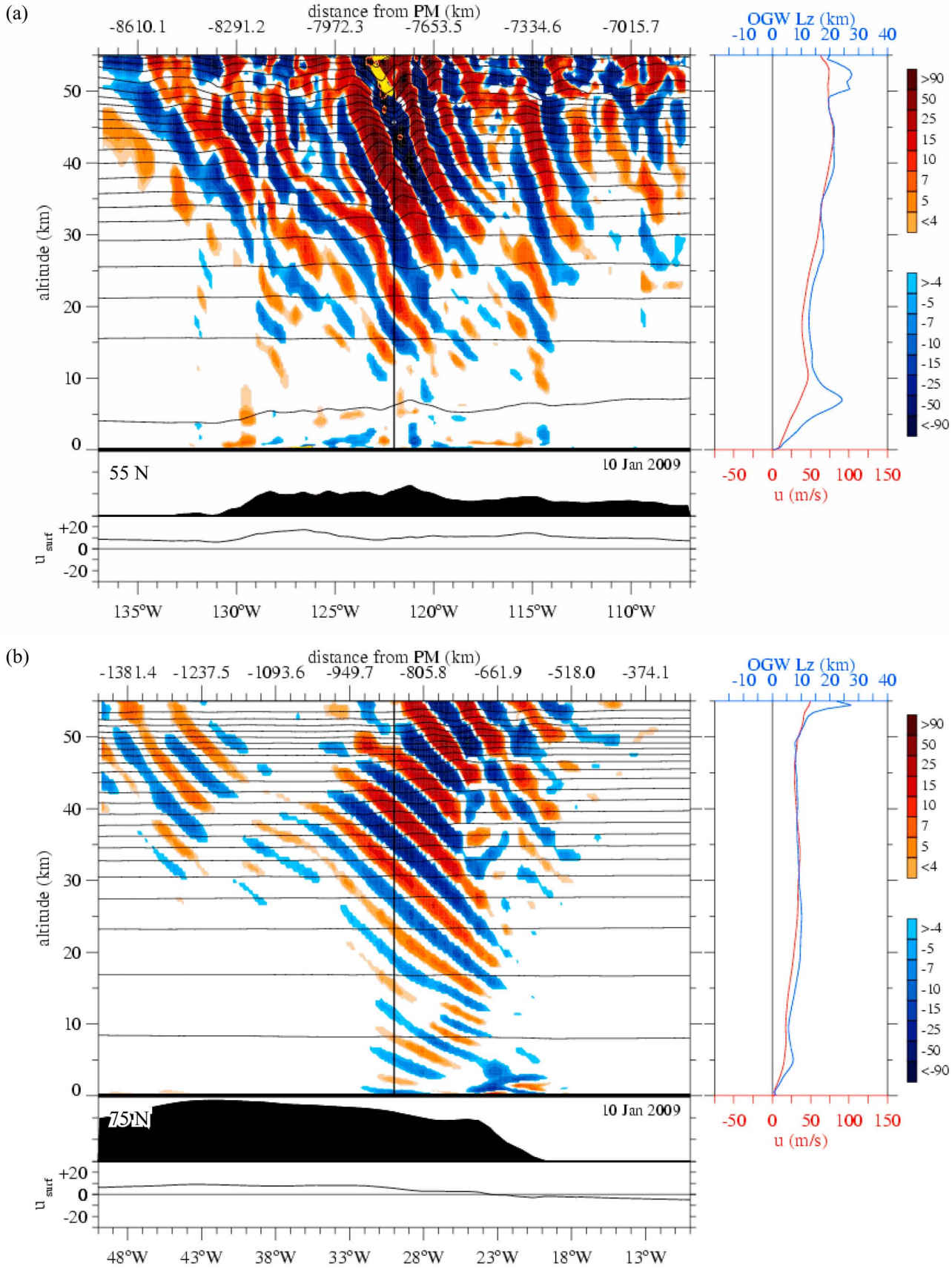
(a)
distance from PM (km)
-8610.1
-8291.2
-7972.3
-7653.5
-7334.6
-7015.7
OGW Lz (km)
-10 0 10 20 30 40
altitude (km)
50
40
30
20
10
0
>90
50
25
15
10
7
5
<4
>-4
-5
-7
-10
-15
-25
-50
<-90
55 N
10 Jan 2009
u surf
+20
0
-20
-50 0 50 100 150
u (m/s)
135°W
130°W
125°W
120°W
115°W
110°W
(b)
distance from PM (km)
-1381.4
-1237.5
-1093.6
-949.7
-805.8
-661.9
-518.0
-374.1
OGW Lz (km)
-10 0 10 20 30 40
altitude (km)
75 N
10 Jan 2009
u surf
+20
0
-20
-50 0 50 100 150
u (m/s)
48°W
43°W
38°W
33°W
28°W
23°W
18°W
13°W

Figure 7

Table 1. Estimates of Wave Properties Based on Vertical Cross Sections Shown in Figure 7

Latitude[a]	Vertical Range (km)	λ_x (km)	L_z (km)	$\lvert f/\omega \rvert$	c_x (m s^{-1})	c_{gz} (km hr^{-1})	u (m s^{-1})	N (s^{-1})
55°N	30–40	160	17.5	0.05	−2.1	22.6	64.17	0.0224
75°N	30–40	125	8.7	0.08	−0.9	8.2	34.04	0.0241

[a]Position corresponds to cross-section position.

from Figure 7), respectively, the ground-relative zonal phase speed is predicted to be small and westward (~−2 m s^{-1}) and an upward vertical group velocity of ~23 km h^{-1}. Table 1 summarizes the GW wave parameters at 55°N and also at 75°N at the longitude marked by the vertical line in Figure 7.

[38] Assuming local zonal propagation of GWs with frequencies larger than the Coriolis parameter (f) but smaller than the buoyancy frequency (N), the GW dispersion relationship can be simplified as [*Andrews et al.*, 1987]

$$c_x - u = -\frac{NL_z}{2\pi}. \tag{4}$$

Here, c_x is the ground-relative phase speed of GWs. When this phase speed approaches the background wind (u), the vertical wavelength (L_z) goes to zero, implying a barrier for vertical propagation. Generally, stratospheric winds favor GWs with opposite phase speeds for vertical propagation. For OGWs, c_x is zero and the vertical wavelength is then given by [e.g., *Eckermann and Preusse*, 1999]

$$(L_z)_{OGW} = 2\pi\frac{u}{N}. \tag{5}$$

[39] The vertical profiles of the OGW vertical wavelength (at the longitudinal location indicated by the vertical line) are shown in blue with the wind profiles (in red) in Figure 7. The estimates of GW vertical wavelength based on the dispersion relationship are similar to the values of the $(L_z)_{OGW}$ profiles averaged in the altitude range, highlighted in Table 1. In particular, the averaged $(L_z)_{OGW}$ values at 55° and 75°N (between 30 and 40 km) are ~17.9 and 8.8 km, respectively. To this end, given the location (topographical feature and near-surface wind), the similarity between the vertical wavelength estimated from the dispersion relationship and the OGW vertical wavelength (equation (5)) suggests that the dominant GWs during 10 January are indeed OGWs.

5.2. SSW Onset of 20 January 2009

[40] Unlike the 10 January case, the global distribution of the vertical flux of zonal momentum on 20 January (Figure 5b) reveals less vertical coherence among the regions of westward propagating GWs at various levels. This change is attributable to the complex environment of alternating westerlies and easterlies (associated with the elongated polar vortex) as evidenced by the zonal mean wind structure (Figure 4b). In particular, the dominant presence of easterly wind between 50°N and 60°N around 50 km tends to filter out westward propagating GWs with relatively slow phase speed. With the weakening of the polar westerly during the SSW onset, we also note more eastward propagating GWs at higher latitude region than during 10 January.

[41] The local effects of zonal wind are further illustrated in Figure 8 which shows the altitude-longitude distribution of GW divergence at 55°N and 75°N for 1200 and 1600 UTC. At 55°N, we see that dominant westward propagating GW features near Eurasia (as demonstrated in Figure 5) are part of a persistent wave packet over the Russian topography with strong near-surface wind (Figures 8a (top) and 8b (top)). In the presence of strong overlying westerly wind (gray shading), wave perturbations grow quite large and potentially undergo wave breaking near the zero wind line around 50 km (as suggested by the yellow areas). The corresponding wave damping would contribute to the decelerative effects around 55°N and 50 km shown in Figure 3 for 20 January which shows the time-averaged, zonal mean easterly wind in the region. At 75°N, two dominant GW packets persist above Novaya Zemlya Island (around 60°E) with strong near-surface westerly wind and around 120°W where the surface westerly wind is relatively weaker (see Figures 8a (bottom) and 8b (bottom)). These wave perturbations extend upward to around 40 km where the background wind switches to easterly.

[42] Figure 9 shows a close-up of the wave packet at 75°N over 120°W at 1200, 1400, and 1600 UTC. Below 30 km, the background wind (u) increases with altitude and the wave perturbations between 113°W and 118°W are quasi-stationary (relative to the ground) and propagate westward relative to the mean flow (as suggested by the negative fluxes in Figure 5). These waves originate very low from the surface and are likely OGWs generated by the strong eastward wind approaching the western Canadian archipelago (as indicated in Figure 8). Based on the diagnosis discussed below, in situ wave source below 30 km related to flow imbalance do not appear to the cause of these perturbations. From equation (5), as u increase with altitude, the vertical

Figure 7. A close-up view of the simulated GW on 10 January (time-averaged) (a) at 55°N and (b) at 75°N. (left) The horizontal divergence is shown as color contours. The underlying terrain is shown as a yellow shape (every tick mark along the ordinate axis represents 1000 km). The zonal wind at the third model level ("u_{surf}") is shown below the terrain. The longitudinal spatial scale is expressed as distance from the Prime Meridian (PM) at the top of each image. Potential temperature is shown as line contours every 100 K, starting from 100 K. (right) At the vertical line, the zonal wind profile is shown in red along with the corresponding theoretical vertical wavelength (L_z) of orographic GW (OGW).

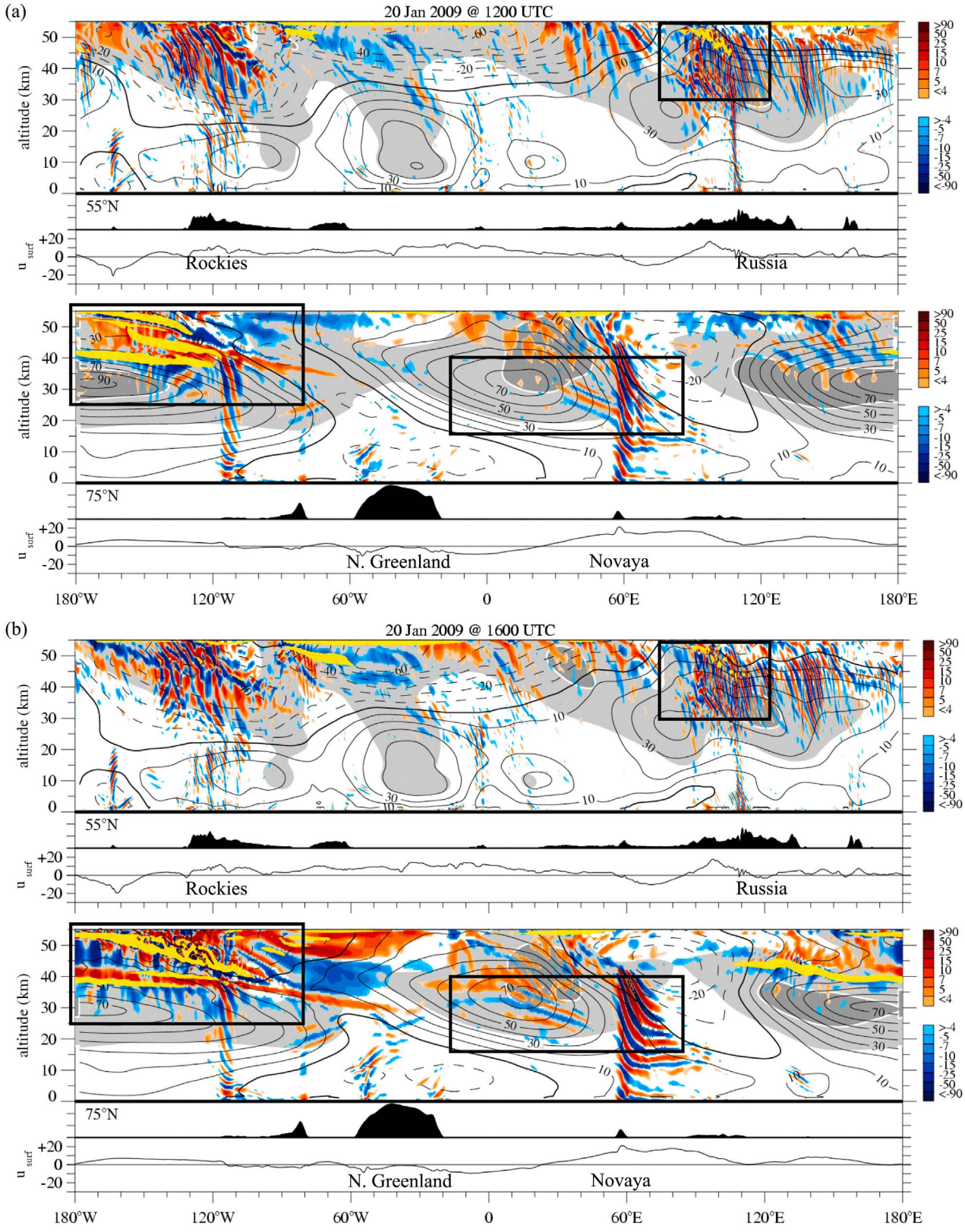

Figure 8. Same as Figure 6 but for 20 January 2009 and for 55°N and 75°N.

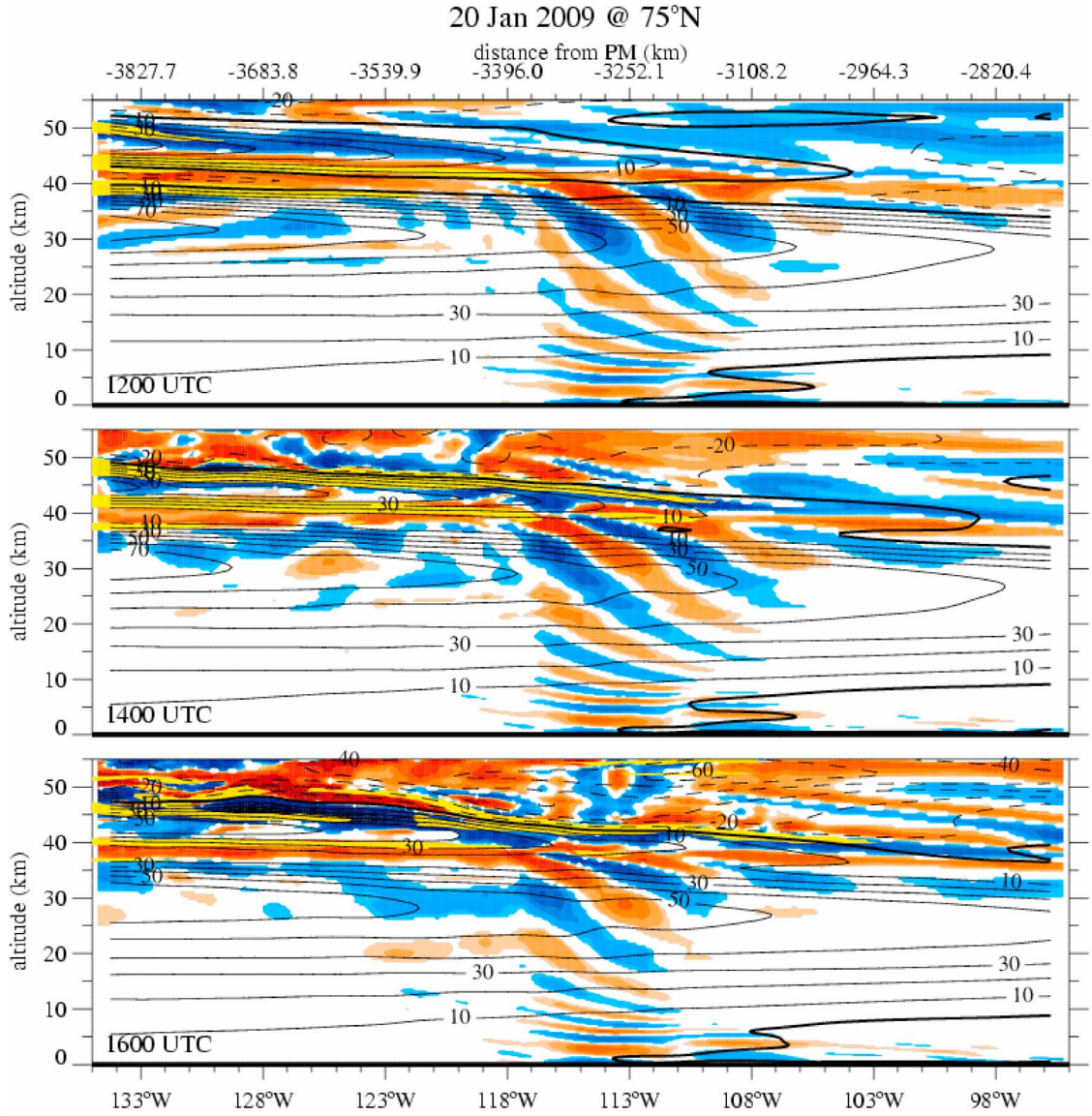

Figure 9. Close-up, altitude-longitude cross-sectional views of 20 January GW near 112°W at (top) 12:00 UTC, (middle) 14:00 UTC, and (bottom) 16:00 UTC. Solid color contours show the horizontal wind divergence with the same color scale as shown in Figure 8. Line contours show zonal wind. Yellow regions indicate areas with $Ri < 0.25$.

wavelength (L_z) tends to increase as seen in Figure 9 by the thickening of alternating blue and orange bands between 20 and 30 km.

[43] Above 30 km, the wind rapidly decreases with altitude and the GW vertical wavelength diminishes. As the mean wind becomes zero around 45 km between 113°W and 118°W, these waves potentially undergo breaking as suggested by the widespread yellow regions near the zero wind line. Although persistent wave patterns are difficult to identify, Figure 5b (right) at 40 km indicates a mixture of eastward and westward propagating GWs in the 120°W, 75°N vicinity. We speculate that the presence of these migrating GWs may be generated by wave breaking process in the upper region of the quasi-stationary packet over the western Canadian archipelago. Based on an idealized, two-dimensional model, *Satomura and Sato* [1999] illustrated that secondary generation of GW can occur in association with OGW dissipation both upstream and downstream of the possible breaking zone. Similarly, observations of *Scavuzzo et al.* [1998] noted enhanced GW features propagating upward and downward from the level where the initial OGWs were large. However, this is difficult to verify in the present three-dimensional simulation since the wave structures are complicated by strong vertical variation, the reversal of the background wind, and potential interference with other waves. We note that similar transient secondary waves may also be present during 10 January above 45 km among the strong OGW packets noted in Figure 6.

[44] At 75°N, a vertically limited wave packet (seen between 20 and 40 km) propagates westward rapidly away

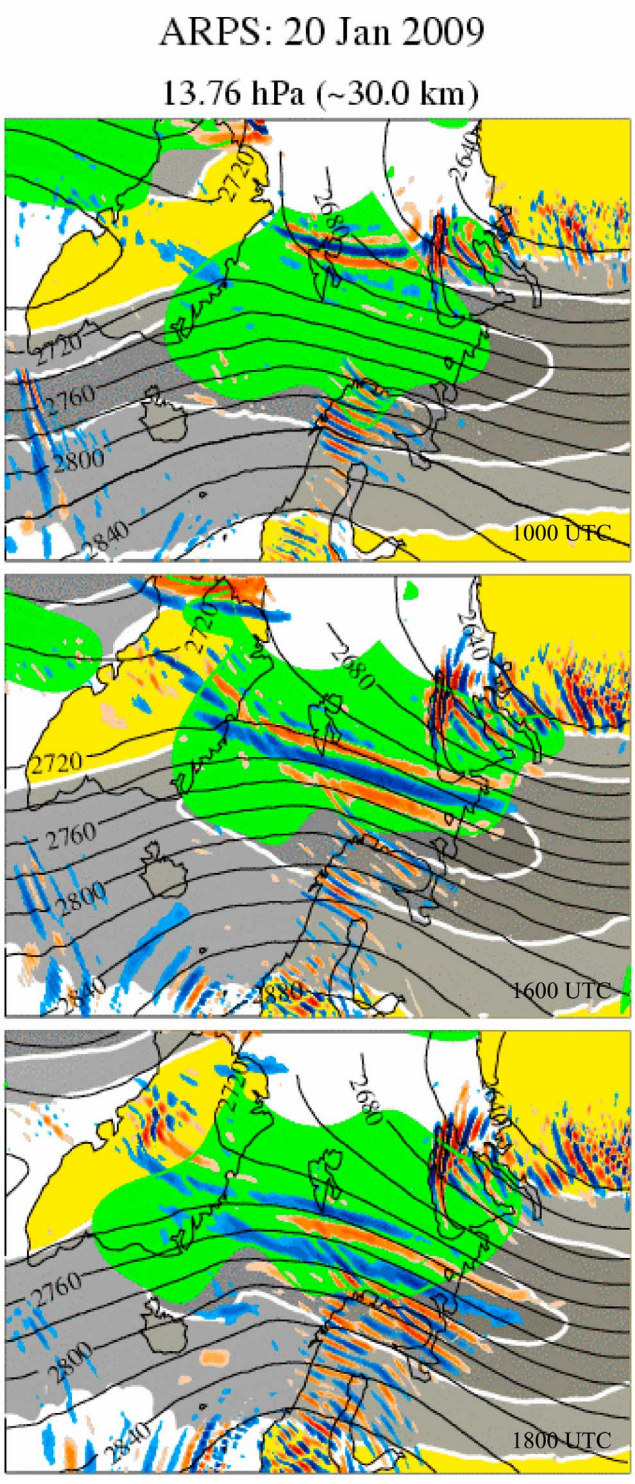

Figure 10. Snapshot, close-up views of 20 January GW near Svalbard (Norway) at (top) 10:00 UTC, (middle) 16:00 UTC, and (bottom) 18:00 UTC. Solid color contours show the horizontal wind divergence with the same color scale as shown in Figure 6. Geopotential heights are plotted as line contours. Green regions represent areas where the ΔNBE exceed 4×10^{-9} s^{-2}. Successive darker gray regions identify areas of strong horizontal wind speed (40, 60, and 80 m s^{-1}).

from the persistent GW packet over Novaya Zemlya (enclosed by the boxes in Figures 8a (bottom) and 8b (bottom)). A close-up of the region centered near the Svalbard at 13.76 hPa (~30 km) reveals that this wave packet exists independently from the persistent wave packet (Figure 10). Indeed, the packet appears north of Svalbard (Norway) at 1000 UTC and propagates southward and westward in time. The packet lies to the west of the quasi-stationary GWs over Novaya Zemlya where the approaching wind is predominantly northerly. A plot of the vertical flux of zonal momentum at 30 km likewise illustrates a localized region of westward propagating GWs near Novaya Zemlya (not shown).

[45] This westward propagating GW packet may be emitted in situ by processes associated with flow imbalance. The wave emission is potentially related to the process in which the atmospheric flow adjusts toward a nonlinear balance state, which is more appropriate than geostrophy in realistic atmosphere [e.g., *Hoskins et al.*, 1985; *McIntyre and Norton*, 2000]. *O'sullivan and Dunkerton* [1995] demonstrated that subsynoptic-scale GW (horizontal wavelength of 600–1000 km) can be spontaneously emitted through unbalanced winds [e.g., *Hartmann*, 2007] as the tropospheric jet stream became distorted by baroclinic instability in a region of wind deceleration. Using a model with very high spatial resolution, *Zhang* [2004] showed that propagating mesoscale GW (horizontal wavelength 100–200 km) can radiate away from the exit region of the jet streak. However, these propagating GW from atmospheric jets are still poorly understood and their wave characteristics and propagation can be quite complex depending on the degree of flow deformation [*Plougonven and Snyder*, 2005]. *Hitchman et al.* [2003] observed rapidly propagating GWs in the vicinity of Severnaya Zemlya during December 1999 and suggested their importance in the formation of polar stratospheric clouds.

[46] Following *Zhang et al.* [2000], we evaluate potential flow imbalance in the simulation results by using the residual term in the nonlinear balance equation (ΔNBE):

$$\Delta NBE = 2J(u,v) - \beta u + f\zeta - \nabla^2\Phi. \qquad (6)$$

Here, u and v are zonal and meridional wind, respectively, and Φ is the geopotential. J is the Jacobian, β is the meridional derivative of the Coriolis parameter (f), and ζ is the relative vorticity. The Jacobian term (J) tends to characterize the horizontal wind shear. The Laplacian ($\nabla^2\Phi$) tends to characterize horizontal wind curvature. As noted by *Zhang et al.* [2000], positive ΔNBE tends to correspond closely to a positive geopotential height anomaly. *Wang and Alexander* [2009] used the magnitude of the ΔNBE diagnostics to correlate enhancement of ΔNBE magnitude to the observed GW variances. Here, the computation is done for both the GEOS data and the simulation results. Both diagnostics yielded similar results since the large-scale flow are similar in both data sets.

[47] Areas where the ΔNBE magnitude exceeds 4×10^{-9} s^{-2} are shown in green in Figure 10. This critical value was arbitrarily chosen based on the values found by *Wang and Alexander* [2009], *Zhang* [2004], and *Sato and Yoshiki* [2008]. Large areas of possible flow imbalance collocate with regions of the strong jet (gray shadings). Near Sval-

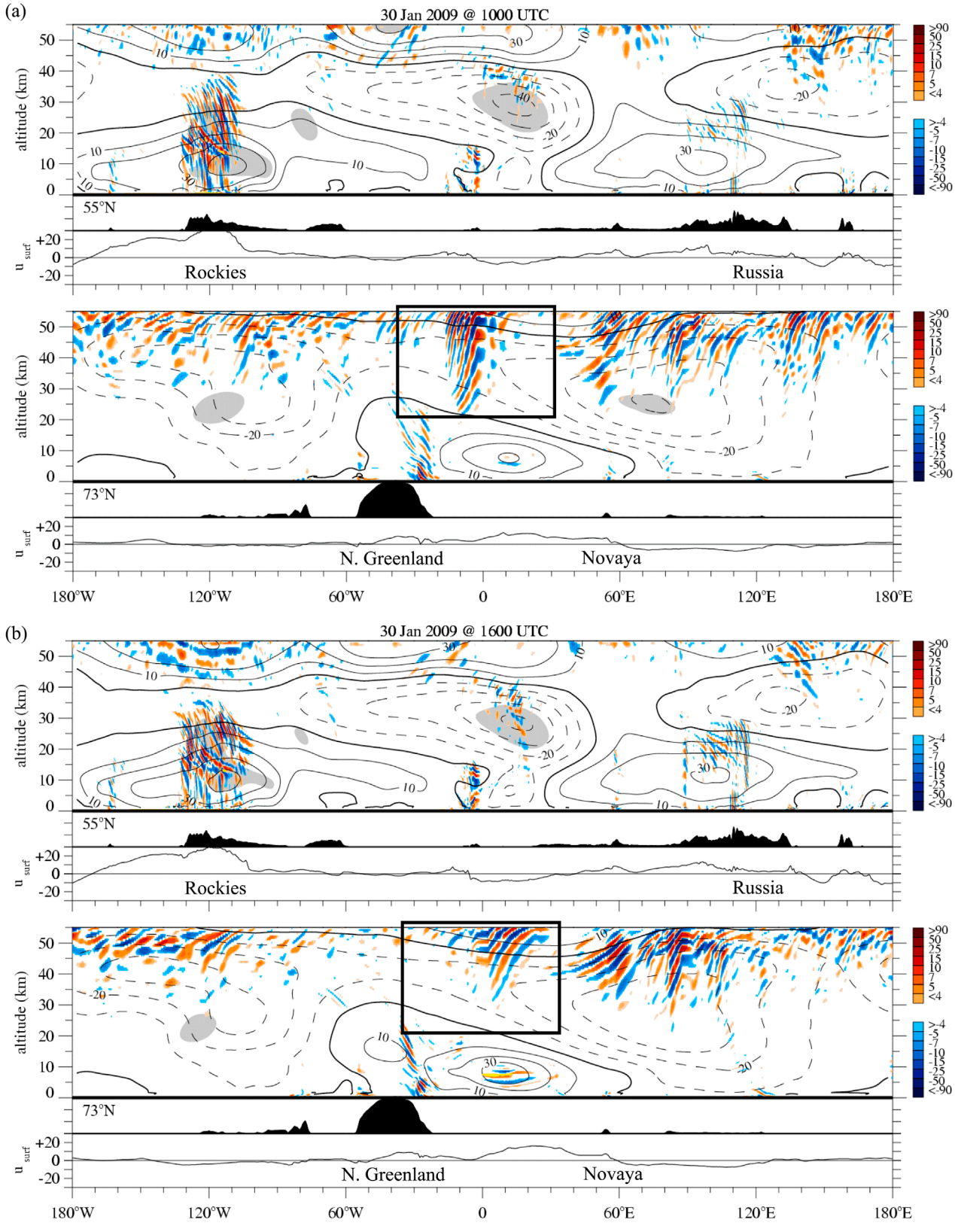

Figure 11. Same as Figure 6 but for 30 January 2009 and for 55°N and 73°N.

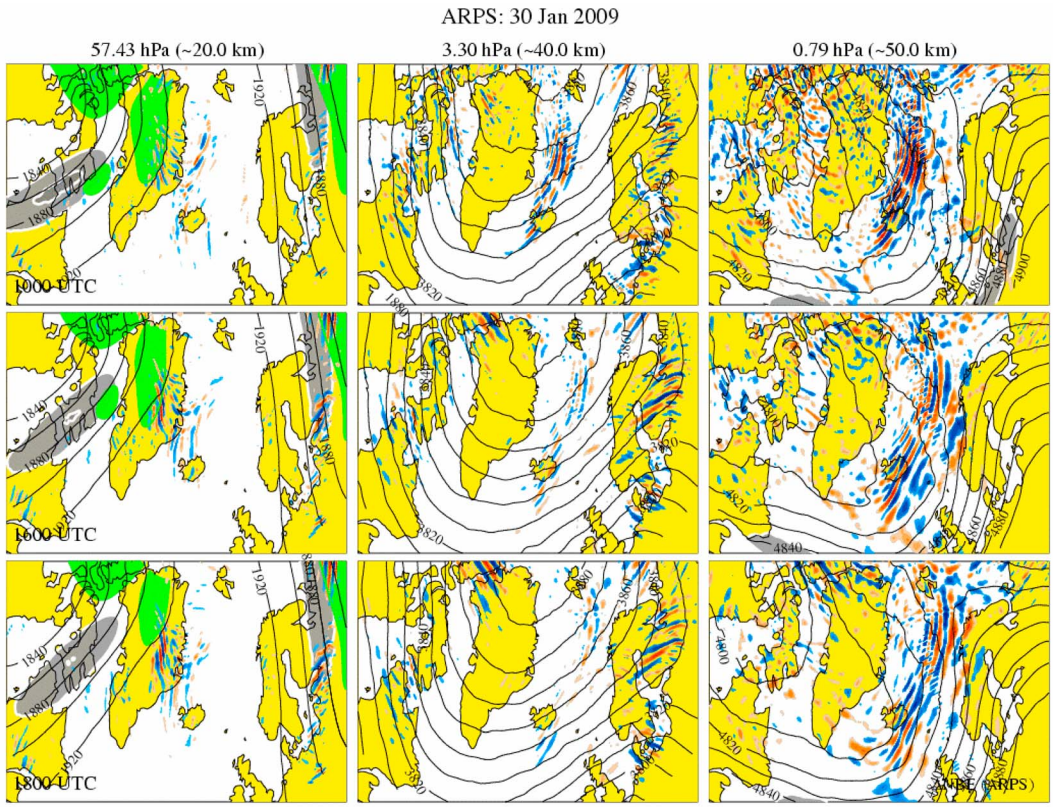

Figure 12. A snapshot, close-up view of 30 January GW near Greenland. Plotting conventions are the same as in Figure 10.

bard, the atmospheric flow experiences strong deformation and local acceleration (as result of the elongated vortex). The coincidence of the radiating GW packet away from Svalbard and the region of strong flow imbalance (and jet strength) suggests spontaneous wave emission by flow adjustment. We note that the ΔNBE diagnostic is applied here for the stratospheric jet. In the literature, its applications have been applied almost exclusively in the tropospheric flow to locate the wave source [*Wang and Alexander*, 2009; *Zhang*, 2004]. However, the diagnostic formulation (as shown above) is based solely on horizontal flow and does not seem to preclude its application in the stratosphere as utilized by *Sato and Yoshiki* [2008].

5.3. Late SSW: 30 January 2009

[48] By 30 January, the overall GW presence is significantly less (and weaker) than during other key dates. Westward propagating GWs are mostly confined below 30 km, as shown in Figures 4d and 5c. These westward propagating features are associated mainly with OGWs over the Rockies and near southern Russia (100°E and 50°N). Altitude-longitude cross section around the 55°N circle (Figure 11) shows the related wave packets in conjunction with relatively strong westerly surface winds (particularly near the Rockies) and how they are limited by the overlying zero wind.

[49] Overall, the entire wind field has considerably weakened and is dominated by easterly wind, consistent with the zonal mean evolution of Figure 1a. Compared to the 10 and 20 January, eastward propagating GWs are the dominant feature above 30 km between 70° and 80°N. At 40 km, the wave activities are found over Norwegian/Greenland Sea (around the Prime Meridian) and near Novaya Zemlya (Figure 5c) and, in a zonal mean sense, are dominated by spatial scale of 100–400 km (Figure 4d). In Figure 11, we clearly see this eastward traveling packet in the altitude-longitude cross section at 73°N as highlighted in the black box (see also Figure 5 at 40 km). In this region, the background wind changes from easterly to westerly from 30 to 55 km. Based on equation (4), as the positive (eastward) GW phase speed approaches the increasing wind profile in this altitude range, the GW vertical wavelength should decrease. This change in the vertical scale is suggested by the eastward "arching" of the wavefronts with altitude near the Prime Meridian.

[50] Close-up plots over Greenland (Figure 12) at multiple levels and instances suggest that the wave packet originates from below 40 km and radiates upward and eastward with altitude. At 57 hPa (~20 km), a region of large ΔNBE magnitude (green) resides near the exit region of strong flow (gray). At 1000 UTC, we see a small band of curved wavefronts appearing just east of the Greenland coast at 20 km, and we can trace the wave packet up through 50 km. As time progresses, the wavefronts become more widespread while propagating away from Greenland. While the overall structure is complicated by interference with other

perturbations, our diagnosis suggests that the propagating GW may have been generated by unbalanced flow adjustment process in the lower stratosphere.

6. Discussions and Summary

[51] In the present paper, we provide an initial look into the possible GW evolution during a dramatic event in the middle atmosphere associated with the 2008–2009 major SSW. This examination is primarily based on a global mesoscale simulations (of 10 km horizontal resolution and 400 m vertical resolution), complemented by analyses and satellite observations. Compared to recent NH winters, the 2008–2009 SSW is chosen for this study due to its relatively clean transition of zonal mean westerly to easterly as the polar region undergoes anomalous warming. The polar vortex in this event undergoes a split, as reflected in the dominance of the zonal wave number 2 planetary scale disturbance. Because of high computation costs, four key dates are selected for high-resolution, 24 h simulations. Each date samples the SSW evolution in January 2009.

[52] Prior to the SSW event (about 10 days before the zonal mean reversal at 60°N), strong GW activity is present around the polar edge as westward propagating wave packets emanate from key topographical features (e.g., the Rockies, Greenland, Russian ranges) up to 55 km (the model's effective upper boundary limit). Nearly stationary relative to the ground, these packets are likely associated with OGWs as suggested by their locations and wave characteristics. In the upper stratosphere, their GW amplitudes can become very large in regions of strong stratospheric wind (i.e., polar edge) and their shorter vertical wavelengths are filtered out by absorption due to the wind. The presence of enhanced GWs along the vortex edge (with strong winds) is consistent with observations of previous SSW, like those by *Duck et al.* [1998, 2001], *Venkat Ratnam et al.* [2004], *Wang and Alexander* [2009], and *Yamashita et al.* [2010]. While PW momentum forcing is relatively weak just prior to SSW, strong westward GW forcing (exceeding 50 m s^{-1} d^{-1}) is quite evident above 40 km throughout the westerly jet core in association with the dissipation of westward propagating GWs (mostly of the 100–400 km horizontal spatial scales). However, a localized region of eastward forcing also exists and may be related to secondary GW generation in very strong winds.

[53] During the SSW onset, OGWs persist at various geographical locations, but tend to be capped at lower levels due to the appearance of the zero wind zonal wind near the upper portion of the model. The zero wind presence is the result of the alternating westward and eastward zonal wind around the North Hemisphere that is related to the emerging wave number-2 planetary disturbance and the vortex elongation. As strong vortex winds are distorted by PW disturbance, possible breaking of OGWs appear to generate secondary, propagating GWs that account for some of the eastward traveling GWs. Other propagating GWs may also result from unbalanced flow adjustment in the middle atmosphere. During this time, the overall GW activity is less than prior to SSW and PWs contribute the largest westward momentum forcing. Regardless, just above the zero wind line, damping of westward propagating GWs exert considerable westward momentum forcing in concert with PW in the emerging, midlatitude easterly jet. The combined westward momentum forcing would give rise to the pronounced downward residual motion over the pole as noted in GEOS (Figure 1b).

[54] As the SSW wanes, GW activities are reduced significantly further. The overall flow weakens as easterly zonal wind becomes widespread. Westward propagating GWs (mainly OGW packets) appear predominantly in the midlatitudes and extend upward just beyond 20 km. With the significant decrease in westward propagating GW disturbance above 20 km, eastward propagating GWs become widespread in the anticyclonic vortex above 30 km. The simulation suggests that unbalanced flow adjustment processes may likewise contribute to these eastward propagating GWs. Following the marked decrease in wave activity, momentum forcings by PW and GW are considerably weaker after the SSW onset. Although westward momentum forcing persists, the wave influence and flux tend to descend in time with the zero wind line.

[55] Concurrent work by *Yamashita et al.* [2010] uses the ECMWF-799 analyses to examine the relationship between GW and PW during the same 2008–2009 SSW. Consistent with the present result, all GW activity in the analyses enhances before the zonal mean wind reversal and significantly weakens after the SSW onset. The analyses show that most GWs occur along the edge of the polar vortex as noted here where the jet is strong [see *Dunkerton and Butchart*, 1984]. Furthermore, the simulations and analyses demonstrate the downward descent of PW forcing and GW perturbations with the zero wind line in time as SSW matures, due to wave–mean flow interactions [*Matsuno*, 1971]. While the PW phase (i.e., the vortex/wind structure) appears to dictate GW variability, the limited time sampling of the present simulations cannot reveal a positive correlation between episodes of GW enhancement and PW amplifications, as suggested by *Yamashita et al.* [2010]. However, resolution differences between the analyses and the simulation may also lead to different GW characteristics when the vortex undergoes strong distortion. Regardless, over the altitude band of 65°N–70°N, we note that spatial scale dominance in GWs during SSW seen in ARPS is consistent with their results despite the limited sampling here. With a horizontal resolution of 10 km, the ARPS can reveal GW features between 50 and 100 km, not resolved by ECMWF-T799. In particular, GWs of these finer scales can be quite strong prior to SSW onset.

[56] Given the three-dimensional nature of the model and the moderately high horizontal and vertical resolution (relative to GCMs and most analyses), the evolution of the simulated GWs can be complicated. These complications arise from variation in the sources (fluctuation in surface winds or jet fluctuation), propagation effects, and wave interferences (other GWs and PWs present in the background). As noted by *Fritts and Alexander* [2003], nonlinearity is a ubiquitous aspect of GW evolution and, while it may be blurred by numerical artifacts and model setup, it can further add to this complication. For example, wave-wave interactions and wave breaking events can induce secondary wave emissions and wave–mean flow interaction can change the background winds in which these waves propagate [*Alexander*, 2010]. These complications will also apply for situations in the real atmosphere. While the

identification of all the possible sources that resulted in the simulated GWs is beyond the scope of this paper, it seems likely that we can exclude convection as a GW source in the present high latitude, wintertime simulation (as suggested by *Richter et al.* [2010]).

[57] We note the ΔNBE diagnostic has been traditionally applied in the troposphere [e.g., *Zhang*, 2004; *Wang and Alexander*, 2009]. However, ΔNBE is based on horizontal flow curvatures so should be applicable at all altitudes. In the stratosphere, where strong wind strength and shear (as well as curvature) can be large (particularly prior to SSWs), NBE values can be very large [e.g., *Sato and Yoshiki*, 2008]. Its application in this paper is very exploratory. Possible improvement over NBE diagnostics may be to examine the local (Lagrangian) wind acceleration in the atmosphere to account for possible in situ unbalanced flow adjustment process (C. Davis, NCAR, personal communication, 2010).

[58] With the large-scale flow well simulated, the GW features in the model may reflect certain wave aspects that occur in reality. Salient characteristics (like vertical wavelength and phase speed) of the simulated GWs appear consistent with the linear GW dispersion relationship, accounting for how changes in the background wind can act to filter GW vertical propagation. As the wave speed approaches the background wind, the simulated GWs tend to have shorter vertical wavelengths. At this point, the present study offers a glimpse into what the detailed GW characteristics may be during drastic vortex evolution. However, given the rapidly changing conditions and the complications discussed above, observational verification of GWs during SSW will be challenging.

[59] **Acknowledgments.** V.L. is supported in part by Large Scale Dynamics Program and Major Research Instrumentation Program at National Science Foundation (NSF) under awards ATM-0646672 and AGS-0958616, respectively, and National Aeronautics and Space Administration (NASA) contract NNX07AR25G. Part of this work was done while V.L. was on sabbatical at National Center for Atmospheric Research (NCAR). Support for M.J.A.'s contribution to this manuscript comes from NSF under award 0943506. Y.O. was supported by Norwegian Research Council (project ARCTIC LIS). Resources supporting this work were provided in part by NASA High-End Computing (HEC) Program through NASA Advanced Supercomputing (NAS) Division at Ames Research Center. Finally, we are greatly indebted to the anonymous reviewers and Matt Hitchman, who provided very helpful suggestions and ideas to greatly improve this paper.

References

Alexander, M. J. (2010), Gravity waves in the stratosphere, in *The Stratosphere: Dynamics, Chemistry, and Transport*, edited by L. M. Polvani, A. Sobel, and D. W. Waugh, *Geophys. Monogr. Ser.*, vol. 190, AGU, Washington, D. C., doi:10.1029/2009GM000887.

Alexander, M. J., S. D. Eckermann, D. Broutman, and J. Ma (2009), Momentum flux estimates for South Georgia Island mountain waves in the stratosphere observed via satellite, *Geophys. Res. Lett.*, *36*, L12816, doi:10.1029/2009GL038587.

Alexander, M. J., et al. (2010), Recent developments in gravity-wave effects in climate models and the global distribution of gravity-wave momentum flux from observations and models, *Q. J. R. Meteorol. Soc.*, *136*, 1103–1124.

Andrews, D. G., J. R. Holton, and C. B. Leovy (1987), *Middle Atmosphere Dynamics*, 490 pp., Academic, San Diego, Calif.

Birner, T., and P. D. Williams (2008), Sudden stratospheric warmings as noise-induced transitions, *J. Atmos. Sci.*, *65*, 3337–3343, doi:10.1175/2008JAS2770.1.

Bloom, S., et al. (2005), Documentation and validation of the Goddard Earth Observing System (GEOS) data assimilation system—Version 5, *NASA Tech. Rep., 104606*, vol. 26, 166 pp.

Charlton, A. J., L. M. Polvani, J. Perlwitz, F. Sassi, E. Manzini, K. Shibata, S. Pawson, J. E. Nielsen, and D. Rind (2007), A new look at stratospheric sudden warming. Part II: Evaluation of numerical model simulations, *J. Clim.*, *20*, 470–488, doi:10.1175/JCLI3994.1.

Charney, J. G., and M. E. Stern (1962), On the stability of internal baroclinic jets in a rotating atmosphere, *J. Atmos. Sci.*, *19*, 159–172, doi:10.1175/1520-0469(1962)019<0159:OTSOIB>2.0.CO;2.

Doyle, J. D., et al. (2000), An intercomparison of model-predicted wave breaking for the 11 January 1972 Boulder windstorm, *Mon. Weather Rev.*, *128*, 901–914, doi:10.1175/1520-0493(2000)128<0901:AIOMPW>2.0.CO;2.

Duck, T. J., J. A. Whiteway, and A. I. Carswell (1998), Lidar observations of gravity wave activity and Arctic stratospheric vortex core warming, *Geophys. Res. Lett.*, *25*, 2813–2816, doi:10.1029/98GL02113.

Duck, T. J., J. A. Whiteway, and A. I. Carswell (2001), The gravity wave–arctic stratospheric vortex interaction, *J. Atmos. Sci.*, *58*, 3581–3596, doi:10.1175/1520-0469(2001)058<3581:TGWASV>2.0.CO;2.

Dunkerton, T. J., and N. Butchart (1984), Propagation and selective transmission of internal gravity waves in a sudden warming, *J. Atmos. Sci.*, *41*, 1443–1460, doi:10.1175/1520-0469(1984)041<1443:PASTOI>2.0.CO;2.

Eckermann, S., and P. Preusse (1999), Global measurements of stratospheric mountain waves from space, *Science*, *286*(5444), 1534–1537, doi:10.1126/science.286.5444.1534.

Fritts, D. C., and M. J. Alexander (2003), Gravity wave dynamics and effects in the middle atmosphere, *Rev. Geophys.*, *41*(1), 1003, doi:10.1029/2001RG000106.

Garcia, R. R., and B. A. Boville (1994), "Downward control" of the mean meridional circulation and temperature distribution of the polar winter stratosphere, *J. Atmos. Sci.*, *51*, 2238–2245, doi:10.1175/1520-0469(1994)051<2238:COTMMC>2.0.CO;2.

Hartmann, D. L. (2007), The atmospheric general circulation and its variability, *J. Meteorol. Soc. Jpn.*, *85B*, 123–143, doi:10.2151/jmsj.85B.123.

Hitchman, M. H., J. C. Gille, C. D. Rodgers, and G. Brasseur (1989), The separated polar winter stratopause: A gravity wave driven climatological feature, *J. Atmos. Sci.*, *46*, 410–422, doi:10.1175/1520-0469(1989)046<0410:TSPWSA>2.0.CO;2.

Hitchman, M. H., M. L. Buker, G. J. Tripoli, E. V. Browell, W. B. Grant, C. Hostetler, T. J. McGee, and J. F. Burris (2003), Nonorographic generation of Arctic polar stratospheric clouds during December 1999, *J. Geophys. Res.*, *108*(D5), 8325, doi:10.1029/2001JD001034.

Holton, J. R. (1983), The influence of gravity wave breaking on the general circulation of the middle atmosphere, *J. Atmos. Sci.*, *40*, 2497–2507, doi:10.1175/1520-0469(1983)040<2497:TIOGWB>2.0.CO;2.

Horinouchi, T. T. N., and J. Kosaka (2002), Convectively generated mesoscale gravity waves simulate throughout the middle atmosphere, *Geophys. Res. Lett.*, *29*(21), 2007, doi:10.1029/2002GL016069.

Hoskins, B. J., M. E. McIntyre, and A. W. Robertson (1985), On the use and significance of isentropic potential vorticity maps, *Q. J. R. Meteorol. Soc.*, *111*, 877–946, doi:10.1256/smsqj.47001.

Leovy, C. B. (1964), Simple models of thermally driven mesospheric circulation, *J. Atmos. Sci.*, *21*, 327–341, doi:10.1175/1520-0469(1964)021<0327:SMOTDM>2.0.CO;2.

Limpasuvan, V., D. L. Wu, M. Joan Alexander, M. Xue, M. Hu, S. Pawson, and J. R. Perkins (2007), Stratospheric gravity wave simulation over Greenland during 24 January 2005, *J. Geophys. Res.*, *112*, D10115, doi:10.1029/2006JD007823.

Limpasuvan, V., J. H. Richter, Y. J. Orsolini, F. Stordal, and O.-K. Kvissel (2011), The roles of planetary and gravity waves during a major stratospheric sudden warming as characterized in WACCM, *J. Atmos. Sol. Terr. Phys.*, doi:10.1016/j.jastp.2011.03.004, in press.

Liu, H.-L., and R. G. Roble (2002), A study of a self-generated stratospheric sudden warming and its mesospheric–lower thermospheric impacts using the coupled TIME-GCM/CCM3, *J. Geophys. Res.*, *107*(D23), 4695, doi:10.1029/2001JD001533.

Manney, G. L., M. J. Schwartz, K. Krueger, M. L. Santee, S. Pawson, J. N. Lee, W. H. Daffer, R. A. Fuller, and N. J. Livesey (2009a), Aura Microwave Limb Sounder observations of dynamics and transport during the record-breaking 2009 Arctic stratospheric major warming, *Geophys. Res. Lett.*, *36*, L12815, doi:10.1029/2009GL038586.

Manney, G. L., et al. (2009b), Satellite observations and modeling of transport in the upper troposphere through the lower mesosphere during the 2006 major stratospheric sudden warming, *Atmos. Chem. Phys.*, *9*, 4775–4795, doi:10.5194/acp-9-4775-2009.

Matsuno, T. (1971), A dynamical model of the stratospheric sudden warming, *J. Atmos. Sci.*, *28*, 1479–1494, doi:10.1175/1520-0469(1971)028<1479:ADMOTS>2.0.CO;2.

McIntyre, M. E., and W. A. Norton (2000), Potential vorticity inversion on a hemisphere, *J. Atmos. Sci.*, *57*, 1214–1235, doi:10.1175/1520-0469(2000)057<1214:PVIOAH>2.0.CO;2.

O'Neill, A., W. L. Grose, V. D. Pope, H. McClean, and R. Swinbank (1994), Transport during 2006 sudden warming: Evolution of the stratosphere during northern winter 1991/92 as diagnosed from U. K. Meteorological Office analyses, *J. Atmos. Sci.*, *51*, 2800–2817, doi:10.1175/1520-0469(1994)051<2800:EOTSDN>2.0.CO;2.

Orsolini, Y. J., J. Urban, D. P. Murtagh, S. Lossow, and V. Limpasuvan (2010), Descent from the polar mesosphere and anomalously high stratopause observed in 8 years of water vapor and temperature satellite observations by the Odin Sub-Millimeter Radiometer, *J. Geophys. Res.*, *115*, D12305, doi:10.1029/2009JD013501.

O'sullivan, D., and T. J. Dunkerton (1995), Generation of inertia-gravity waves in a simulated life cycle of baroclinic instability, *J. Atmos. Sci.*, *52*, 3695–3716, doi:10.1175/1520-0469(1995)052<3695:GOIWIA>2.0.CO;2.

Pawson, S. (1997) Effects of gravity wave drag in the Berlin troposphere-stratosphere-mesosphere GCM, in *Gravity Wave Processes: Their Parametrization in Global Climate Models*, *NATO ASI Ser., Ser. 1*, vol. 50, edited by K. Hamilton, pp. 327–336, Springer, New York.

Plougonven, R., and C. Snyder (2005), Gravity waves excited by jets: Propagation versus generation, *Geophys. Res. Lett.*, *32*, L18802, doi:10.1029/2005GL023730.

Randel, W. J. (1987), The evaluation of winds from geopotential height data in the stratosphere, *J. Atmos. Sci.*, *44*, 3097–3120, doi:10.1175/1520-0469(1987)044<3097:TEOWFG>2.0.CO;2.

Ren, S., S. M. Polavarapu, and T. G. Shepherd (2008), Vertical propagation of information in a middle atmosphere data assimilation system by gravity-wave drag feedbacks, *Geophys. Res. Lett.*, *35*, L06804, doi:10.1029/2007GL032699.

Richter, J. H., F. Sassi, and R. R. Garcia (2010), Towards a physically based gravity wave source parameterization, *J. Atmos. Sci.*, *67*, doi:10.1175/2009JAS3112.1.

Rienecker, M. M., et al. (2008), The GEOS-5 data assimilation system–Documentation of versions 5.0.1, 5.1.0, and 5.2.0, *NASA Tech. Memo., NASA/TM–2008–104606*, Vol. 27, 102 pp.

Sato, K. (2000), Sources of gravity waves in the polar middle atmosphere, *Adv. Polar Upper Atmos. Res.*, *14*, 233–240.

Sato, K., and M. Yoshiki (2008), Gravity wave generation around the polar vortex in the stratosphere revealed by 3-hourly radiosonde observations at Syowa station, *J. Atmos. Sci.*, *65*, 3719–3735, doi:10.1175/2008JAS2539.1.

Sato, K., T. Kumakura, and M. Takahashi (1999), Gravity waves appearing in a high-resolution GCM simulation, *J. Atmos. Sci.*, *56*, 1005–1018, doi:10.1175/1520-0469(1999)056<1005:GWAIAH>2.0.CO;2.

Sato, K., S. Watanabe, Y. Kawatani, Y. Tomikawa, K. Miyazaki, and M. Takahashi (2009), On the origins of mesospheric gravity waves, *Geophys. Res. Lett.*, *36*, L19801, doi:10.1029/2009GL039908.

Satomura, T., and K. Sato (1999), Secondary generation of gravity waves associated with the breaking of mountain waves, *J. Atmos. Sci.*, *56*, 3847–3858, doi:10.1175/1520-0469(1999)056<3847:SGOGWA>2.0.CO;2.

Scavuzzo, C. M., M. A. Lamfri, H. Teitelbaum, and F. Lott (1998), A study of the low-frequency inertio-gravity waves observed during the Pyrénées Experiment, *J. Geophys. Res.*, *103*, 1747–1758, doi:10.1029/97JD02308.

Schwartz, M. J., W. G. Read, and W. V. Snyder (2006), Polarized radiative transfer for Zeeman-split oxygen lines in the EOS MLS forward model, *IEEE Trans. Geosci. Remote Sens.*, *44*(5), 1182–1191, doi:10.1109/TGRS.2005.862267.

Tomikawa, Y. (2010), Persistence of easterly wind during major stratospheric sudden warmings, *J. Clim.*, *23*, 5258–5267, doi:10.1175/2010JCLI3507.1.

Venkat Ratnam, M., T. Tsuda, C. Jacobi, and Y. Aoyama (2004), Enhancement of gravity wave activity observed during a major Southern Hemisphere stratospheric warming by CHAMP/GPS measurements, *Geophys. Res. Lett.*, *31*, L16101, doi:10.1029/2004GL019789.

Wang, L., and M. J. Alexander (2009), Gravity wave activity during stratospheric sudden warmings in the 2007–2008 Northern Hemisphere winter, *J. Geophys. Res.*, *114*, D18108, doi:10.1029/2009JD011867.

Watanabe, S., K. Sato, and M. Takashi (2006), A general circulation model study of orographic gravity waves over Antarctica excited by katabatic winds, *J. Geophys. Res.*, *111*, D18104, doi:10.1029/2005JD006851.

Watanabe, S., Y. Kawatani, Y. Tomikawa, K. Miyazaki, M. Takahashi, and K. Sato (2008), General aspects of a T213L256 middle atmosphere general circulation model, *J. Geophys. Res.*, *113*, D12110, doi:10.1029/2008JD010026.

Waters, J. W., et al. (2006), The Earth Observing System Microwave Limb Sounder (EOS MLS) on the Aura satellite, *IEEE Trans. Geosci. Remote Sens.*, *44*(5), 1075–1092, doi:10.1109/TGRS.2006.873771.

Wu, D. L. (2004), Mesoscale gravity wave variances from AMSU-A radiances, *Geophys. Res. Lett.*, *31*, L12114, doi:10.1029/2004GL019562.

Xue, M., K. K. Droegemeier, and V. Wong (2000), The Advanced Regional Prediction Systems (ARPS)—A multiscale nonhydrostatic atmospheric simulation and prediction tool. Part I: Model dynamics and verification, *Meteorol. Atmos. Phys.*, *75*, 161–193, doi:10.1007/s007030070003.

Xue, M., D. Wang, J. Gao, and K. K. Droegemeier (2003), The Advanced Regional Prediction System (ARPS), storm-scale numerical weather prediction and data assimilation, *Meteorol. Atmos. Phys.*, *82*, 139–170, doi:10.1007/s00703-001-0595-6.

Yamashita, C., H.-L. Liu, and X. Chu (2010), Gravity wave variations during the 2009 stratospheric sudden warming as revealed by ECMWF-T799 and observations, *Geophys. Res. Lett.*, *37*, L22806, doi:10.1029/2010GL045437.

Zhang, F. (2004), Generation of mesoscale gravity waves in upper-tropospheric jet-front systems, *J. Atmos. Sci.*, *61*, 440–457, doi:10.1175/1520-0469(2004)061<0440:GOMGWI>2.0.CO;2.

Zhang, F., S. E. Koch, C. A. Davis, and M. L. Kaplan (2000), A survey of unbalanced flow diagnostics and their applications, *Adv. Atmos. Sci.*, *17*(2), 165–183, doi:10.1007/s00376-000-0001-1.

M. J. Alexander, Colorado Research Associates Division, Northwest Research Associates, 3380 Mitchell Ln., Boulder, CO 80301, USA.

V. Limpasuvan, Department of Applied Physics, Coastal Carolina University, PO Box 261954, Conway, SC 29528, USA. (var@coastal.edu)

Y. J. Orsolini, Norwegian Institute for Air Research, PO Box 100, Kjeller N-2027, Norway.

J. H. Richter and C. Yamashita, National Center for Atmospheric Research, PO Box 3000, Boulder, CO 80307, USA.

D. L. Wu, Jet Propulsion Laboratory, California Institute of Technology, 4800 Oak Grove Dr., Pasadena, CA 91109, USA.

M. Xue, Center for Analysis and Prediction of Storms, University of Oklahoma, NWC 120 David Boren Blvd., Norman, OK 73072, USA.